NOAA Climate Test Bed

NASA Goddard Space Flight Center

Georgia Institute of Technology

Atmospheric and Environmental Research

Unified Modeling

Seamless Prediction

Integrated Services

Office of Science and Technology

NOAA's National Weather Service

2011

Office of Science and Technology
National Weather Service
National Oceanic and Atmospheric Administration
U.S. Department of Commerce

Table of Content

Decadal Climate Variability and Change in the Mediterranean Region

Annarita Mariotti

Climate Program Office
NOAA's Office of Oceanic and Atmospheric Research, Silver Spring, Maryland

ABSTRACT

The Mediterranean region is among the "Hot Spots" projected to experience major climatic changes in the twenty-first century as a result of the global increase in greenhouse gas (GHG) concentrations. However the way in which these changes may initially become manifest in the Mediterranean will also depend on internal decadal variability and its impacts on climate in this region. Here, we present an analysis of the main decadal climate variations that have influenced past climatic conditions in the Mediterranean/South Europe region since the mid-nineteenth century. Decadal variability is discussed in the context of forced climatic changes from increased GHG.
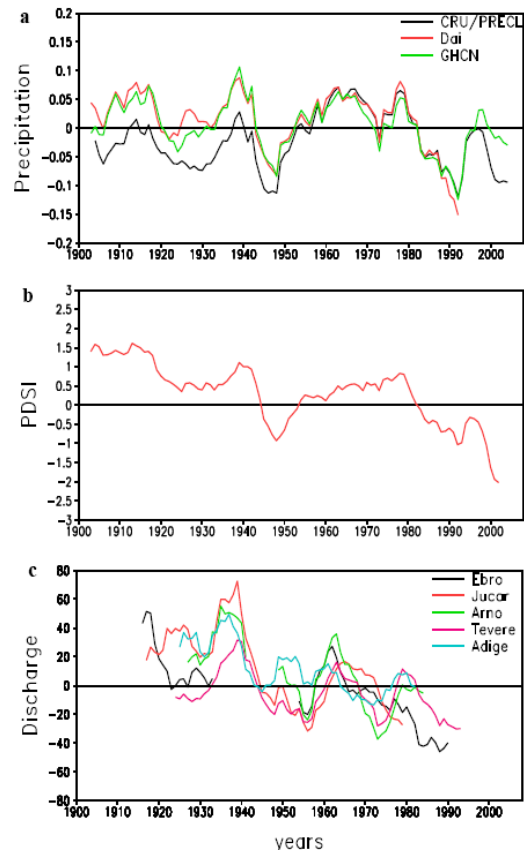
Results point to significant connections between Mediterranean climate and decadal and multi-decadal variability in the Atlantic. Namely, a significant influence of the North Atlantic Oscillation on Mediterranean precipitation and a relationship between regional temperatures and the Atlantic Multi-decadal Oscillation which may imply a certain degree of decadal regional predictability. CMIP3 projections indicate that in the longer term "forced" regional climatic changes from GHG increases would bring significantly drier conditions over land and major changes in Mediterranean Sea water cycle.

---

1. Observed twentieth century changes

An analysis of observed twentieth century long-term changes in the water cycle of Mediterranean land areas is presented by Mariotti et al. (2008) (see Figure 1). A weak albeit significant long-term negative precipitation trend is found over Mediterranean land areas. The Palmer Drought Severity Index (PDSI), which reflects the combined effects of precipitation and surface temperature changes, shows a progressive and substantial drying of Mediterranean land surface since 1900 consistent with a decrease in precipitation and an increase in surface temperature. The inter-decadal PDSI fluctuations are similar to those of precipitation, with wetter 1960s compared to the drier 1940s.

Consistently with PDSI behaviour, a number of Mediterranean rivers for which long-time series are available also show long-term decreases in discharge during the

Fig. 1 Mediterranean water cycle changes observed during the 20th century relative to the period 1950-2000. Area-averaged annual mean precipitation anomalies (six-years running means) from various datasets (panel a; mm/d) and PDSI (panel b; a.u.); discharge anomalies (units are % of climatology) for various Mediterranean rivers (panel c). Due to data availability, discharge anomalies are relative to the 1960-1980 period. From [Mariotti *et al.*, 2008].

Correspondence to: Annarita Mariotti, Climate Program Office, NOAA's Office of Oceanic and Atmospheric Research, Silver Spring, Maryland; E-mail: Annarita.Mariotti@noaa.gov

twentieth century. Such river discharge decreases are likely in part due to intensified water use.

2. Role of the North Atlantic Oscillation

The linkages between decadal variability of seasonal precipitation (DVSP) anomalies over the Mediterranean and the NAO are explored in Figure 2 (see Mariotti and Dell'Aquila, 2011). In DJF, Mediterranean-mean DVSP anomalies evoke a SLP correlation pattern clearly reminiscent of the NAO, a well known major influence on Mediterranean precipitation during winter (i.e. a positive NAO tends to correspond to drier conditions in the Mediterranean and vice-versa). This connection at decadal time-scales is confirmed by the spatial correlation of the NAO index with DJF precipitation in the Mediterranean domain. Based on this map, the NAO explains over 25% - 30% of decadal DJF precipitation variance in a region spanning parts of Spain, Marocco, Southern France, Italy and the Balkans. The NAO has been shown to affect Mediterranean precipitation by modulating SLP directly over the Mediterranean and by reorganizing large-scale moisture fluxes into the region [Mariotti and Arkin, 2007]. Drier (wetter) decades in the Mediterranean largely correspond to higher (lower) than usual regional SLP and to a positive (negative) NAO phase. The correlation of decadal variability of JJA precipitation anomalies in the Mediterranean with the Summer North Atlantic Oscillation (SNAO) of [Folland *et al.*, 2009] is also shown in Fig.2. The SNAO has significant positive correlation with JJA precipitation in Italy and parts of the Balkans, explaining up to 25% - 30% of decadal precipitation variability in these regions.

Fig. 2 Influence of large-scale decadal climate modes on Mediterranean precipitation over the period 1850-2009. A)-B) Correlation of Mediterranean-mean DVSP anomalies with SLP anomalies in the Euro-Atlantic sector over the period 1901-2000 for DJF (panel A) and JJA (panel B). C)-D) Correlation of DVSP anomalies in the Mediterranean region with various climatic indices: DJF precipitation and NAO (panel C); JJA precipitation and SNAO (panel D). E)-F) Decadal variation of Mediterranean-mean seasonal anomalies of precipitation, SLP and various climatic indices: DJF precipitation, SLP and NAO (panel E; note the sign of the NAO index is reversed); JJA precipitation and SNAO (panel F). In all, anomalies, relative to 1901-2000, are de-trended and time-filtered using 10-year running mean. In panels A-D, a black contour encloses areas where the correlation is above the 95%.

3. Linkages with the Atlantic Multi-decadal oscillation

An analysis of the linkages between decadal variability of surface air temperature (Ta) anomalies in the Mediterranean and in surrounding regions is shown in Figure 3. In JJA Mediterranean-mean Ta presents a coherent pattern of positive correlation with surface air temperature in the North Atlantic, with highest values in the eastern North Atlantic off the North African and European coasts. The correlation of Ta over the North Atlantic/European sector with the Atlantic Multidecadal Oscillation index shows that in JJA the AMO/Ta pattern over the Atlantic extends to parts of western Europe and the Mediterranean. This is in stark contrast with what is found in DJF, when the AMO correlation pattern is confined to the North Atlantic with no significant correlation with Ta over Europe, nor the Mediterranean (compare Fig. 3 C-D). The analysis of
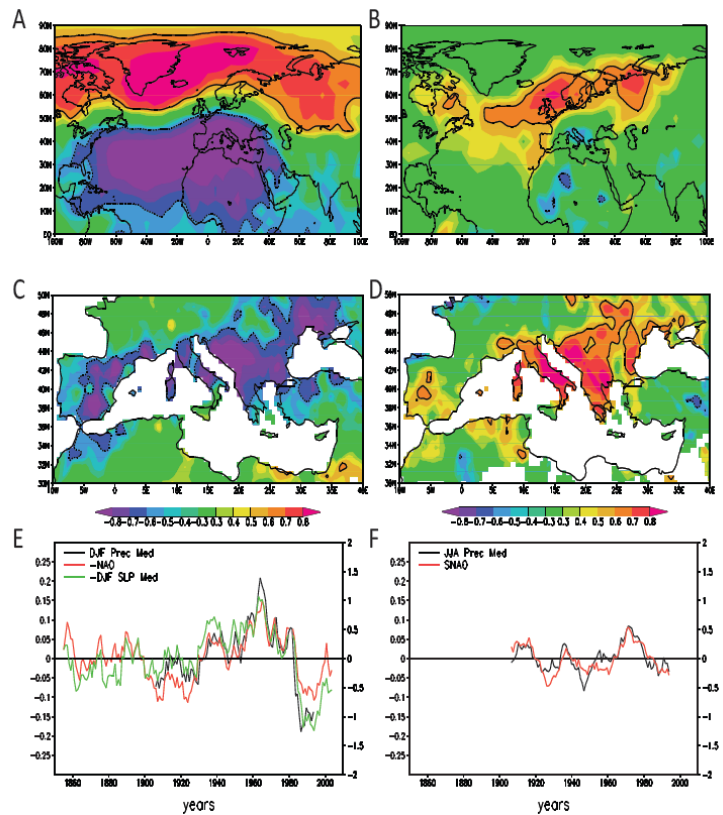
Mediterranean-mean decadal variability of Ta anomalies also shows contrasting characteristics in JJA and DJF: multi-decadal AMO-like Ta variations in JJA (Mediterranean-mean Ta/AMO index correlation is 0.77 over the period 1850-2009); decadal variation of the anomalies, with no-AMO correlation in DJF (compare Fig. 3 E-F). Interestingly, Mediterranean SST significantly correlate with AMO variability throughout the year.

4. "Forced" Mediterranean water cycle changes

Mariotti *et al.*, 2008 study Mediterranean water cycle changes associated with modifications in radiative forcing based on an ensemble of multi-model coupled simulations from the WCRP Coupled Model Intercomparison Project Phase 3 (hereafter CMIP3). Twentieth century simulations, using observed radiative forcings (both natural and anthropogenic), give a progressive "forced" decrease in rainfall in the Mediterranean region during this century, somewhat higher than that derived from observational data (see section 1). CMIP3 simulations also show a tendency for Mediterranean Sea evaporation and E-P water budget to increase toward the end of

Fig. 3 Influence of large-scale decadal climate modes on Mediterranean surface air-temperature over the period 1850-2009. A)-B) Correlation of decadal Mediterranean-mean land surface air temperature (CRUTEM) anomalies with large-scale surface air temperature anomalies (HadCRU) for DJF (panel A) and JJA (panel B). C)-D) Correlation of decadal surface air temperature anomalies (HadCRU) with the AMO index for DJF (panel C), and JJA (panel D). E)-F) Time series of decadal Mediterranean-mean land surface air temperature (CRUTEM), Mediterranean SST and the AMO index for DJF (panel E) and JJA (panel F). In all, anomalies are relative to 1901-2000; values are detrended and time-filtered using 10-year running mean. In panels A-D, a black contour encloses areas where the correlation is above the 95% significance level. Mariotti and Dell'Aquila, 2011.

the twentieth century in response to the radiative forcings (see Fig. 4).

Based on an ensemble of CMIP3 twenty-first century SRES-A1B emission scenario simulations, Mariotti *et al.* (2008) show that the above mentioned simulated twentieth century precipitation decrease would be followed by a rapid drying from 2020 onwards. Evapotranspiration would also decrease because of the drier land surface, but, as increased surface temperature favours higher evaporation, the rate would be half that of precipitation. While the "forced" drying found by Mariotti *et al.* (2008) over land is large, projected changes for the Mediterranean Sea are even more dramatic. Unlike the surrounding land region where evaporation decreases, the projected precipitation reduction over the sea is accompanied by a roughly equal increase in evaporation due to increased sea surface temperature (SST) (ultimately due to more energy input from greenhouse warming). The projected increase in the loss of freshwater (E-P) at the sea surface towards the end of the twenty-first century is large, roughly equal to what is typically received in total by the Mediterranean Sea on an annual basis as discharge from neighboring land and as inflow from the Black Sea.

5. Discussion

Although there is a high degree of inter-model consistency among the CMIP3 models regarding Mediterranean climate projections, uncertainties need to be carefully evaluated. These include general uncertainties associated with CMIP3 projections due to model errors (*e.g.* limited model resolution or the
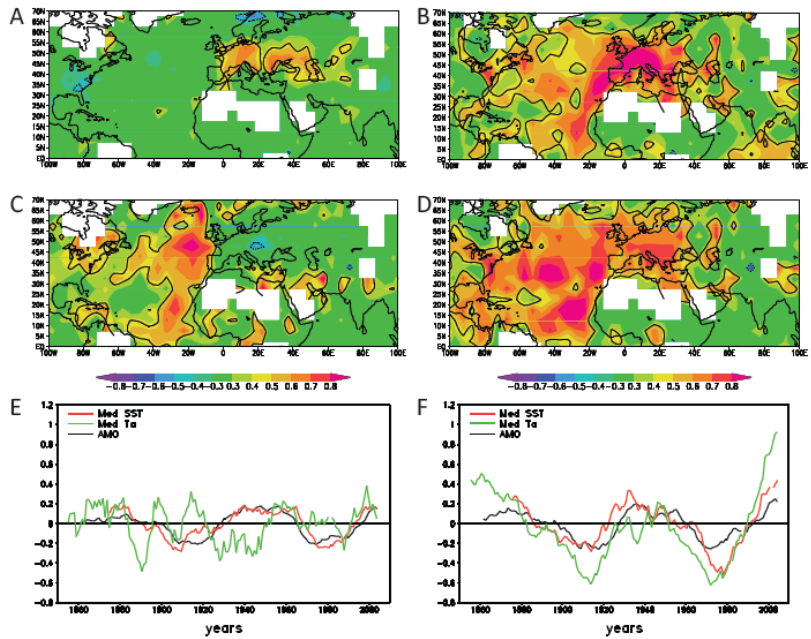
parameterisation of physical processes), the effects of "internal" variability (from purely atmospheric modes or modes of coupled interactions within the ocean-atmosphere-land system) and uncertainties in future emission paths and natural radiative forcings (*e.g.*, future volcanic eruptions). The uncertainty in emission paths is likely to play a larger role later in the twenty-first century when differences among scenarios become larger. In addition to the above mentioned general uncertainties, there are also region-specific uncertainties, including potential errors and limitations in the CMIP3 models' representation of regional climate variability, Mediterranean Sea circulation and regional climate feedbacks.

The role of "internal" variability on future water cycle variations can be best understood by looking at past regional water cycle variability and comparing this with the results from the CMIP3 twentieth century simulations. Observational analyses of twentieth century water cycle variability in this region show long-term trends including a tendency for increased surface aridity and increased Mediterranean Sea evaporation. These changes are not inconsistent with the "forced" changes depicted by the CMIP3 simulations as a result of green-house gas concentrations increases during this century. However, observational precipitation and

Fig. 4 Mediterranean water cycle anomalies over the period 1900-2100 relative to 1950-2000. Area-averaged evaporation (brown), precipitation (blue) and precipitation minus evaporation (black; P-E) are based on an average of CMIP3 model runs. For P-E, the envelope of individual model anomalies and the 1 standard deviation interval around the ensemble mean are also shown (light grey and dark grey shading respectively). Data are six-years running means of annual mean area-averages over the box of Figure 3 broadly defining the Mediterranean region. (Panel a) Land-only. (Panel b) Sea-only. Focus periods are highlighted (yellow). From [Mariotti *et al.*, 2008].

evaporation records also include decadal variations that are larger than the above-mentioned simulated long-term trends (*e.g.* for precipitation, observed decadal anomalies are about two orders of magnitude larger than the simulated trend). As much as both observational errors and model errors can contribute to this discrepancy, this also highlights the important role of "internal" variability in determining observed decadal anomalies. Hence, at least in the short term (roughly 10-30 years out), regional decadal anomalies and any potential for decadal predictability is likely to be critically dependent on the regional impacts of decadal modes of variability "internal" to the climate system.

References

Mariotti, A. and A. Dell'Aquila, 2011: Decadal climate variability in the Mediterranean region: roles of large-scale forcings and regional processes. *Climate Dyn.*, published on-line.
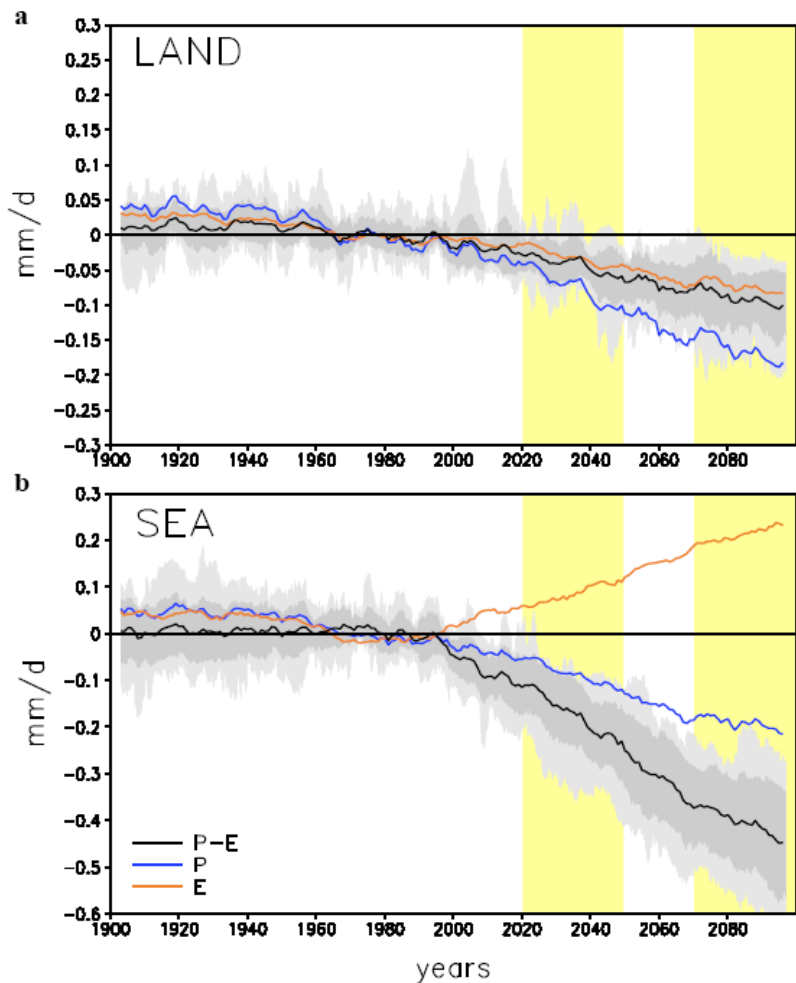
Anav, A., and A. Mariotti, 2011: Projected changes in 21st century Euro-Mediterranean dominant vegetation types. *Climate Res.*, in press.

Mariotti, A., 2010: Recent changes in Mediterranean water cycle: A pathway toward long-term regional hydroclimatic change? *J. Climate*, **23**, 1513-1525.

Sanchez-Gomez, E., S. Somot, and A. Mariotti, 2009: Future changes in the Mediterranean water budget projected by an ensemble of regional climate models. *Geophys. Res. Lett.*, **36**, L21401.

Mariotti, A., N. Zeng, J. Yoon, V. Artale, A. Navarra, P. Alpert, and L. Z X Li, 2008: Mediterranean water cycle changes: transition to drier 21st century conditions in observations and CMIP3 simulations. *Environ. Res. Lett*, **3**, 044001 (8pp) doi:10.1088/1748-9326/3/4/044001.

Mariotti, A., and P. Arkin, 2007: The North Atlantic Oscillation and oceanic precipitation variability. *Climate Dyn.*, **28(1)**, 35-51. DOI: 10.1007/s00382-006-0170-4.

Asymmetric Global Warming: Day versus Night

Liming Zhou

School of Earth and Atmospheric Sciences
Georgia Institute of Technology, Atlanta, Georgia

One distinct climate feature associated with global warming is the widespread decrease of diurnal temperature range (DTR) that has been observed over land since 1950 due to a larger warming in minimum air temperature (T_{min}) than in maximum air temperature (T_{max}). Although the warming trend of mean surface air temperature and the decreasing trend of DTR are closely related, the former has been largely attributed to anthropogenic forcing while the latter to increased cloud cover. The question remains as to what is primarily responsible for the observed DTR decrease and whether this decrease is attributable to human activities. This seminar tries to address this question with three case studies.

The first case study focuses on analyzing spatial patterns of observed annual T_{max}, T_{min} and DTR trends from 1950-2004 and their association with precipitation and cloud cover. It presents observational evidence for a larger DTR decreasing trend and a stronger T_{min} warming trend over drier regions. The grid boxes at spatial resolution of 5° by 5° degrees were classified into a number of large-scale climate regions in terms of the climatological annual precipitation amount at each grid box. The regional average trends of annual T_{min} and DTR exhibit significant spatial correlations with the regional averaged annual precipitation, while such correlation for T_{max} is very weak (Fig. 1). In general, the magnitude of the downward trend of DTR and the warming trend of T_{min} decreases with increasing precipitation amount, *i.e.*, stronger DTR decreasing trends over drier regions. Such spatial dependence of T_{min} and DTR trends on the climatological precipitation possibly reflects large-scale effects of increased global greenhouse gases and aerosols (and associated changes in cloudiness, soil moisture, and water vapor) during the later half of the 20th century.
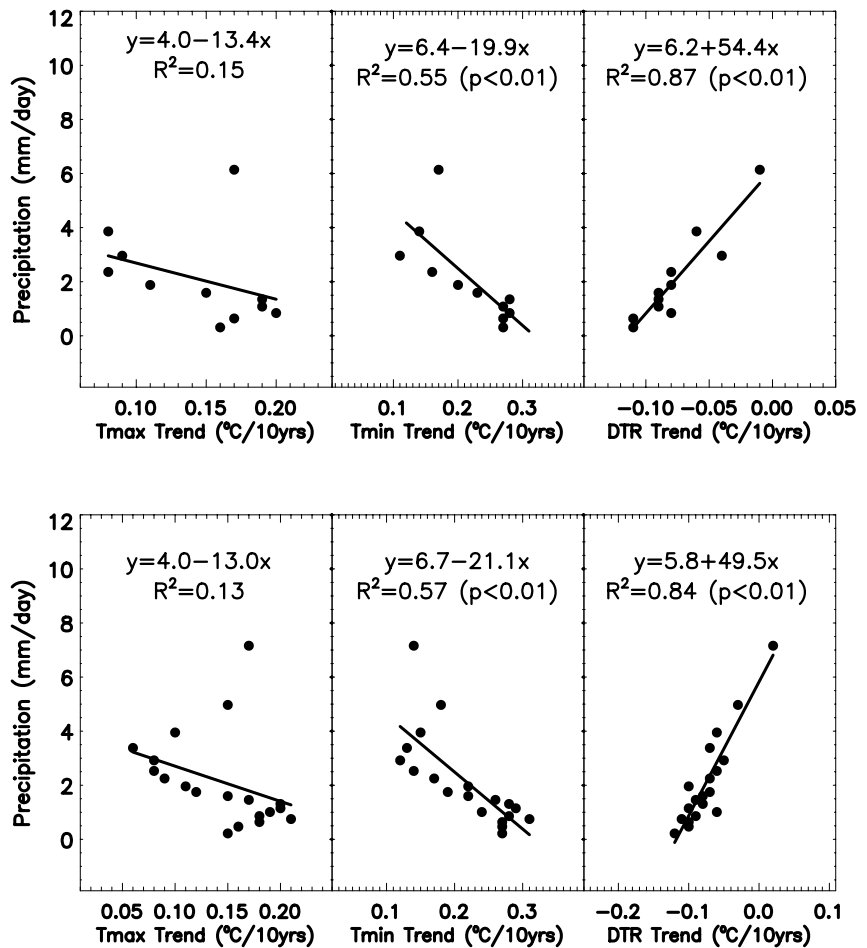

Fig. 1 Spatial dependence of regional average trends of annual T_{max}, T_{min} and DTR on regional average climatological annual precipitation by large-scale climate region during the period 1950-2004. Here only the results for the classifications of 11 (upper panels) and 19 (lower panels) climate regions are shown. A linear regression line was fit between the precipitation and temperature trends.

_____

Correspondence to: Liming Zhou, School of Earth and Atmospheric Sciences, Georgia Institute of Technology, Atlanta, Georgia; E-mail: liming.zhou@eas.gatech.edu

The second case study focuses on comparing the trends and variability in T_{max}, T_{min}, and DTR over land in observations with 48 simulations from 12 global coupled atmosphere-ocean GCMs for the later half of the 20th century. When anthropogenic and natural forcings (referred to as ALL) are included, the models generally reproduce observed major features of the warming of T_{max} and T_{min} and the reduction of DTR (Fig. 2). The greenhouse gases enhanced surface downward longwave radiation (DLW) explains most of the warming of T_{max} and T_{min} while decreased surface downward shortwave radiation (DSW) due to increasing aerosols and water vapor contributes most to the decreases in DTR in the models. When only natural forcings (referred to as NAT) are used, none of the observed trends are simulated (Fig. 2). The simulated DTR decreases are much smaller than the observed (mainly due to the small simulated T_{min} trend) but still outside the range of natural internal variability estimated from NAT. The much larger observed decrease in DTR suggests the possibility of additional regional effects of anthropogenic forcing that the models cannot realistically simulate, likely connected to changes in cloud cover, precipitation, and soil moisture. The small magnitude of the simulated DTR trends may be attributed to the lack of an increasing trend in cloud cover and deficiencies in characterizing aerosols and important surface and boundary-layer processes in the models.

Our results also indicate that the models generally reproduce the spatial dependence of T_{min} and DTR trends on
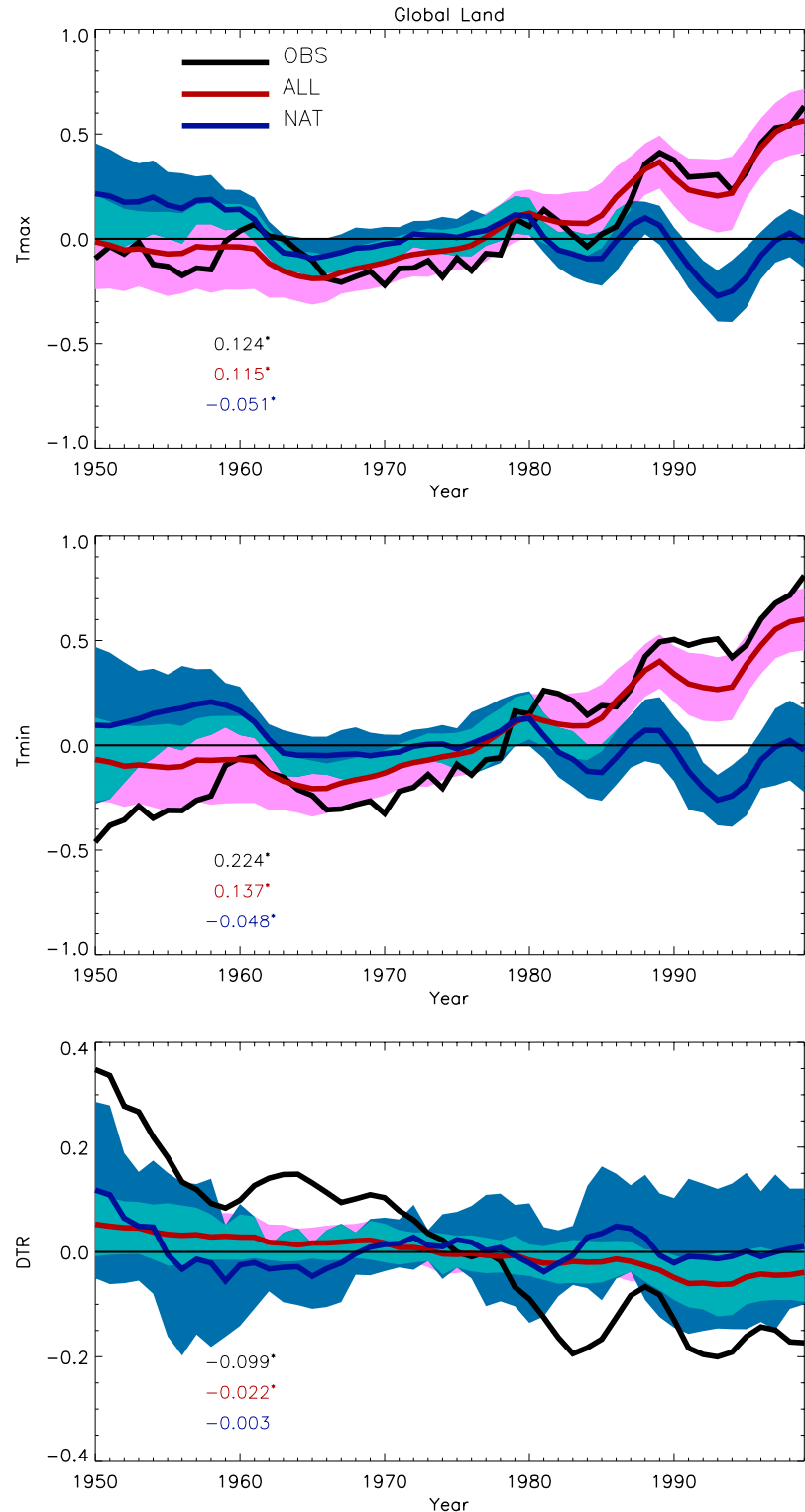

Fig. 2 Annual T_{max} (top), T_{min} (middle) and DTR (bottom) anomalies relative to the mean of period 1961-1990 averaged over global land, as observed (in black) and as obtained from multi-model mean simulations in ALL (red) and NAT (blue) for the period 1950-1999. Shaded regions represent one standard deviation in ALL and NAT and those in light blue represent the overlap between ALL and NAT. The magnitudes of linear trends are listed and those marked with "*" are statistically significant (p<0.05). A 5-point (i.e., 5-year) running averaging was applied for visualization purpose only, with the first and last two year values applied as recycling boundary condition.

the precipitation (Fig. 3) in response to anthropogenic forcings in ALL, but not in NAT (also see the observations in Fig. 1).

The third case study focuses on quantifying feedbacks of changing land surface properties on DTR in a climate model. Observations show that the DTR was reduced most in dry regions and especially in the West African Sahel during a period of unprecedented drought. Furthermore, the negative trend of DTR in the Sahel appears to have stopped and may have reversed after the rainfall began to recover. This study develops a new hypothesis with climate model sensitivity studies showing that either a reduction in vegetation cover or a reduction in soil emissivity would reduce the DTR by increasing T_{min} through increased soil heating and reduced outgoing longwave radiation (Fig. 4). Consistent with empirical analyses of observational data, our results suggest that vegetation removal and soil aridation would act to reduce the DTR during periods of drought and human mismanagement over semiarid regions such as the Sahel and to increase the DTR with more rainfall and better
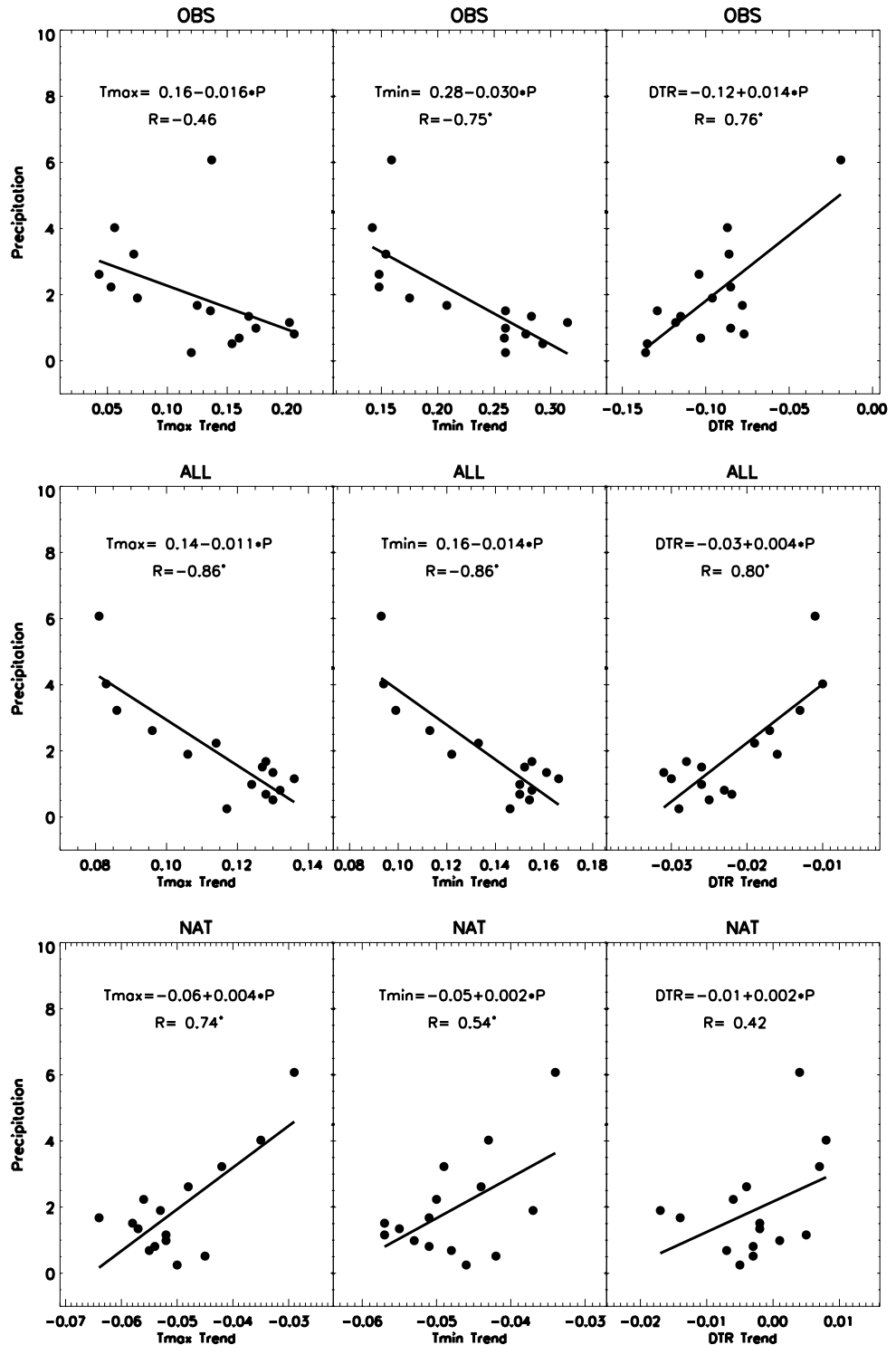

Fig. 3 Spatial dependence of regional average linear trends (°C/10yrs) of annual T_{max} (left), T_{min} (center) and DTR (right) on regional average climatological precipitation in observations (top) and simulations of ALL (middle) and NAT (bottom) in terms of large-scale climate regions during the period 1950-1999. Here only the results for the classification of 15 climate regions are shown. A linear regression line was fit between the precipitation and temperature trends. The correlation coefficients (R) are listed and those marked with "*" are statistically significant (p<0.05).

human management. Other mechanisms with similar effects on surface energy balance, such as increased nighttime downward longwave radiation due to increased greenhouse gases, aerosols, and clouds, would also be expected to have a larger impact on DTR over drier regions.
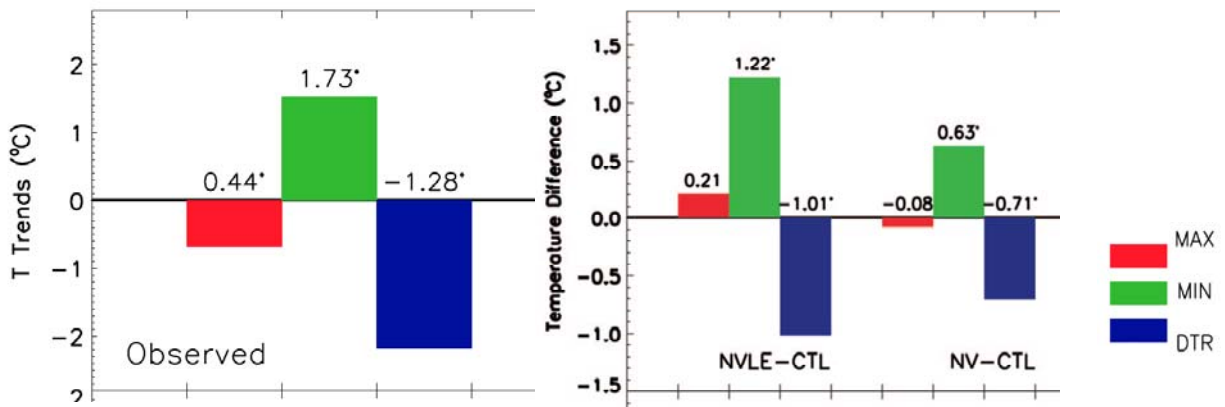

Fig. 4 Left panel: observed linear trends of annual mean T_{max}, T_{min}, and DTR (°C/10yrs) for the period 1950-2004 (left) averaged over the Sahel. Right panel: simulated annual mean T_{max}, T_{min}, and DTR differences (°C) between two experiments (NVLE: no vegetation + lower emissivity, NV: no vegetation) and the control run (CTL) under clear-sky conditions averaged over the Sahel. The temperature trends or differences masked with "*" are statistically significant at the 5% level.

References

Zhou, L., R.E. Dickinson, Y. Tian, R. Vose, and Y. Dai, 2007: Impact of vegetation removal and soil aridation on diurnal temperature range in a semiarid region - application to the Sahel. *Proc Natl Acad Sci USA*, **104**(46), 17937–17942.

Zhou, L., A. Dai, Y. Dai, R.S. Vose, C.-Z. Zou, Y. Tian, and H. Chen, 2009: Spatial patterns of diurnal temperature range trends on precipitation from 1950 to 2004. *Clim Dyn.,* **32**, 429–440. doi: 10.1007/s00382-008-0387-5.

Zhou, L., R.E. Dickinson, P. Dirmeyer, A. Dai, and S.-K. Min, 2009: Spatiotemporal patterns of changes in maximum and minimum temperatures in multi-model simulations. *Geophys Res Lett.* **36**, L02702. doi:10,1029/2008GL036141

Zhou, L., R.E. Dickinson, A. Dai, and P. Dirmeyer, 2010: Detection and attribution of anthropogenic forcing to diurnal temperature range changes from 1950 to 1999: Comparing multi-model simulations with observations. *Clim Dyn,* **35**, 1289–1307. doi:10.1007/s00382-009-0644-2.

Eurasian Snow Cover Variability and Links with Stratosphere-Troposphere Coupling and Their Potential Use in Seasonal to Decadal Climate Predictions

Judah Cohen

Atmospheric and Environmental Research, Inc., Lexington, MA

ABSTRACT

Over a decade of research has allowed us to understand how variability in Siberian snow cover, mostly in October, can influence the weather in remote regions including the Eastern US and Europe months later. Below we describe the six-step model with a timeline that begins with the advance of Siberian snow cover in October and ends with more (less) frequent Arctic outbreaks during the winter in the Eastern US, Europe and East Asia associated with the negative (positive) phase of the large-scale telconnection pattern the Arctic Oscillation (AO). This link has been demonstrated for year-to-year variability and used to improve seasonal-timescale winter forecasts; however this coupling can also be shown to have influenced recent decadal-scale temperature trends.

1. Introduction

Snow cover exhibits the greatest temporal and spatial variability of any other land surface condition (Cohen 1994). Correlations between observed snow cover with sea level pressure (SLP), 500 hPa and standard climate indices all show a significant snow-climate statistical relationship concentrated in the North Atlantic. In Figure 1, Eurasian October snow cover anomalies are correlated with December, January, February (DJF) surface temperature anomalies. The resultant anomaly pattern resembles the Arctic Oscillation (AO) pattern of variability. The AO is an index that measures the pressure gradient between high- and mid-latitudes and is linked to the frequency of Arctic outbreaks in the mid-latitudes. Cohen and Entekhabi (1999) hypothesize that

Fig. 1 a) Regression of DJF land surface temperatures from NCEP/NCAR reanalysis onto the standardized inverted DJF AO index (top). b) As in a) but for regression onto the standardized October Eurasian snow cover index (bottom). Units are in °C.

a possible dynamical mechanism linking Eurasian snow anomalies and North Atlantic climate variability is through the strength and position of the Siberian high. Using a proxy index for the AO, Cohen *et al.* (2001) showed that the winter AO in the lower troposphere originates as a lower tropospheric height anomaly in
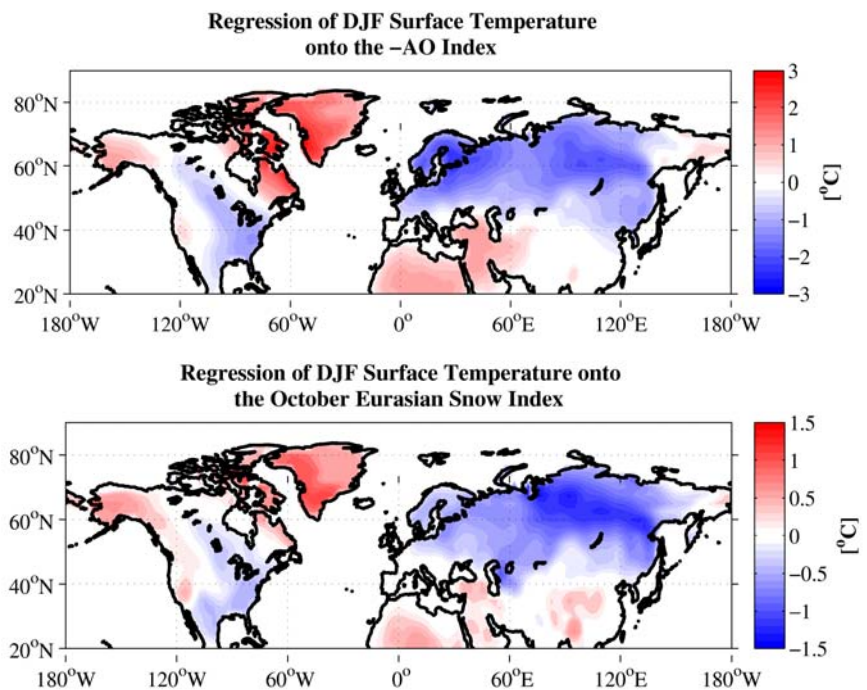
Siberia during the fall. Persistent positive SLP anomalies and negative surface temperature anomalies in the region of Siberia, as early as October, were found to precede a negative winter AO. This provided a further link of the hemispheric scale AO to origins with the inception of the Siberian high in the fall.

We have operationally produced real-time winter forecasts for the extratropical Northern Hemisphere based on fall Eurasian snow cover and atmospheric anomalies for over a decade. The operational forecasts continue to demonstrate skill, up through the most recent winter season. These snow-based forecasts and hindcasts appear to provide considerable additional information beyond the standard-ENSO based forecasts and even the most sophisticated dynamical models (Cohen and Fletcher 2007).

2. Conceptual model

We outline a conceptual model of the dynamical pathway demonstrated by the statistically significant relationship between snow and the winter AO discussed

Fig. 2 Conceptual model for how fall snow cover modifies winter circulation in both the stratosphere and the troposphere. Case for extensive snow cover on right: 1. Snow cover increases rapidly in the fall across Siberia, when snow cover is above normal diabatic cooling helps. 2. to strengthen the Siberian high and leads to below normal temperatures. 3. Snow forced diabatic cooling in proximity to high topography of Asia increases upward flux of energy in the troposphere, which is absorbed in the stratosphere. 4. Strong convergence of WAF indicates higher geopotential heights, a weakened polar vortex and warmer down from the stratosphere into the troposphere all the way to the surface. 6. Dynamic pathway culminates with strong negative phase of the Arctic Oscillation at the surface. Also shown is case for low snow cover on left.

above (Figure 2). October is the month snow cover makes its greatest advance, mostly across Siberia. October is also the month that the Siberian high, one of the three dominant centers of action across the Northern Hemisphere (NH), forms. In years when snow cover is above normal this leads to a strengthened Siberian high and colder surface temperatures across Northern Eurasia in the fall. We suggest that the intensification of the Siberian high, along with the thermal impacts of enhanced snow cover and topographic forcing, corresponds to a positive wave activity flux anomaly in the late fall and early winter, leading to stratospheric warming and to the January tropospheric negative winter AO response we have mentioned above.

a) Snow cover advance

The month when snow cover extent makes its greatest advance is in October. The variability in October snow cover extent from year to year can be very large, with the highest years having a snow cover extent twice or even three times as great as the lowest years. Snow cover has the highest reflectivity or albedo of all naturally occurring surfaces. The presence of snow cover can increase the amount of sunlight reflected back into space from 20 to 80% (Cohen and Rind 1991). Also snow cover is a good insulator or a thermal blanket, preventing heat form the ground escaping into the atmosphere. These radiative properties of snow cover cool the atmosphere above the earth's surface. The presence of snow cover can lead to much colder temperatures than the absence of snow cover.
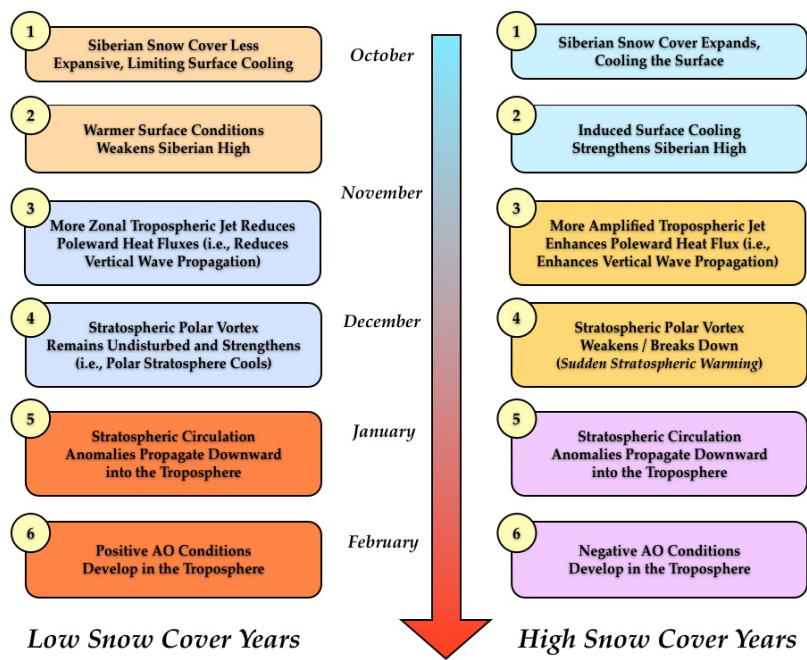
b) Formation of the Siberian high

The presence or absence of snow cover can lead to colder or warmer air masses. When snow cover extent is above normal this cools the overlying atmosphere. Cold-dense air above the snow cover promotes high pressure while warm more buoyant air above a snow free surface promotes low pressure.

During the fall when snow cover rapidly advances across Siberia, the Siberian high starts to form. If snow cover extent is above normal this favors a stronger and more expansive Siberian high. During those falls when snow cover is more extensive, anomalous high pressure is more common stretched across Northern Eurasia. Then during the winter the high-pressure anomalies first limited to northern Eurasia spread across the Arctic Ocean. Simultaneously, high-pressure anomalies dominate the mid-latitude ocean basins. This pattern of sea level pressure variability is recognizable to climatologists as the negative phase of the AO. During the negative phase, high pressure is increased at high latitudes while low pressure is strengthened at mid-latitudes decreasing the pressure gradient between these two regions. Once again a regional perturbation in the fall across Northern Eurasia grows into a hemispheric pattern of variability in the winter.

However when snow cover is below normal across Siberia, this favors the occurrence of predominately low-pressure anomalies across Northern Eurasia during the fall. Then during the winter the low pressure anomalies first limited to northern Eurasia spread across the Arctic Ocean. Simultaneously, low-pressure anomalies dominate the midlatitude ocean basins. This pattern of sea level pressure variability is recognizable to climatologists as the positive phase of the AO. During the positive phase, low pressure is strengthened at high latitudes while high pressure is increased at mid-latitudes increasing the pressure gradient between these two regions. A regional perturbation in the fall across Northern Eurasia grows into a hemispheric pattern of variability in the winter.

The fall sea level pressure precursors not only affect the weather near the earth's surface but they also impact the weather in the stratosphere, the layer of atmosphere between 10 and 50 km above the earth's surface. These fall tropospheric precursors, as we refer to them, initiate anomalous energy transfer from the troposphere to the stratosphere that impacts the winter polar vortex, which we are now discovering plays an important role in the sensible winter weather across the Eastern US, Europe and East Asia.

c) Vertical transfer of energy

The vertical transfer of energy in the atmosphere can have important impacts on the weather across the entire Northern Hemisphere. We have shown an important connection between snow cover extent in Siberia, the strength of the Siberian high and energy transfer in the atmosphere.

During the fall a rapid advance in snow cover favors a strengthened and a more expansive Siberian high. We have shown that a stronger Siberian high can increase the amount of energy transfer from the troposphere or the lower atmosphere to the stratosphere or upper atmosphere. Less snow cover and a weakened Siberian high can lead to a decreased amount of energy transfer from the troposphere to the stratosphere.

Often when the transfer of energy from the troposphere to the stratosphere is increased that excess energy is absorbed in the polar stratosphere. That increase in energy absorption leads to a warming of the polar stratosphere and a weakening of the polar vortex. Warming of the polar stratosphere is often very dramatic and is referred to as a sudden stratospheric warming (SSW). The polar vortex is a fast stream of air that flows west to east around the Pole and it derives its energy from the strong temperature gradient between the equator and the Pole in the stratosphere. During a SSW, the pole to equator temperature gradient is weakened and consequently the polar vortex also weakens. Alternatively, if the transfer of energy from the troposphere to the stratosphere is less, the polar stratosphere cools and the stronger pole to equator temperature gradient strengthen the polar vortex.

d) Changes in the polar vortex

Often when the polar vortex is strong, temperatures are mild in the mid-latitudes across the Eastern US and Northern Eurasia; and when the vortex is weak, temperatures tend to be cold across the Eastern US and northern Europe and Asia.

Strong is the more common state of the polar vortex. When the polar vortex is strong, this creates strong low pressure in the Arctic region. Because of the pressure difference between the Arctic and mid-latitudes, air flows into low pressure and this confines the cold air to high latitudes closer to the Arctic. Therefore it is often mild across the Eastern US, Europe and East Asia during winters when the polar vortex is strong. When there is less transfer of energy from the troposphere to the stratosphere the polar vortex remains strong. During strong polar vortex, the airflow is fast and in a direction from west to east. Low pressure in the Arctic region is referred to as the positive phase of the AO.

When there is more transfer of energy from the troposphere to the stratosphere the polar vortex becomes perturbed. When the polar vortex is weak or "perturbed," the flow of air is weaker and meanders north and south (rather than west to east). This allows a redistribution of air masses where cold air from the Arctic spills into the mid-latitudes and warm air from the subtropics is carried into the Arctic. This mixing of air masses also favors more storms and snow in the mid-latitudes. During a weak polar vortex, high pressure occurs in the Arctic region and is referred to as the negative phase of the AO. Air flows away from the high pressure Arctic. The north to south direction of the polar vortex carries cold Arctic air into the mid-latitudes of Eastern US, Europe and East Asia. Therefore it is cold across the Eastern US, Europe and East Asia during winters when the polar vortex is weak.

e) Downward propagation

When the stratospheric polar vortex is strong this leads to lower heights/pressures in the stratospheric Arctic. These same circulation anomalies then occur in the troposphere all the way down to the surface. With low pressure dominating the Arctic and the Jet Stream poleward of its climatological position, this results in the positive phase of the AO and less frequent Arctic outbreaks into the mid-latitudes and a warmer than normal winter in the Eastern US, Europe and East Asia.

Instead when the stratospheric polar vortex is weak this leads to higher heights/pressures in the stratospheric Arctic. These same circulation anomalies then occur in the troposphere all the way down to the surface. With high pressure dominating the Arctic and the Jet Stream equatorward of its climatological position, this results in the negative phase of the AO and more frequent Arctic outbreaks into the mid-latitudes and a colder than normal winter in the Eastern US, Europe and East Asia.

f) Winter Arctic Oscillation

The forced changes by above (below) normal Siberian snow cover in the atmosphere culminates with an extended period of cold (warm) temperatures across the Eastern United States and Northern Eurasia that dominate the winter mean temperatures.

During the fall a rapid advance in snow cover favors a strengthened and a more expansive Siberian high, which leads to increased energy transfer from the lower to the upper atmosphere and a weakened polar vortex. The cycle ends with the negative phase of the AO. During the negative phase of the AO high pressure dominates the Arctic and the Jet stream shifts southward. Also meridional or north-south flow of air increases. This allows for Arctic air masses to penetrate further south than usual into the midlatitudes while warm subtropical air can reach the Arctic.

In contrast, a slower advance in snow cover favors a weaker and a more contracted Siberian high, which leads to decreased energy transfer from the lower to the upper atmosphere and a strengthened polar vortex. The cycle ends with the positive phase of the AO. During the positive phase of the AO, low pressure dominates the Arctic and the Jet stream shifts northward. Also the meridional or north-south flow of air weakens. This keeps the air masses at different latitudes separated so that cold air remains confined to the Arctic and mild air sweeps across the mid-latitudes.

3. Decadal variability

This snow-AO relationship has been demonstrated for year-to-year variability and is used to improve seasonal-timescale winter forecasts; however, this coupling may be modulating the winter warming trend, with implications for decadal-scale temperature projections.
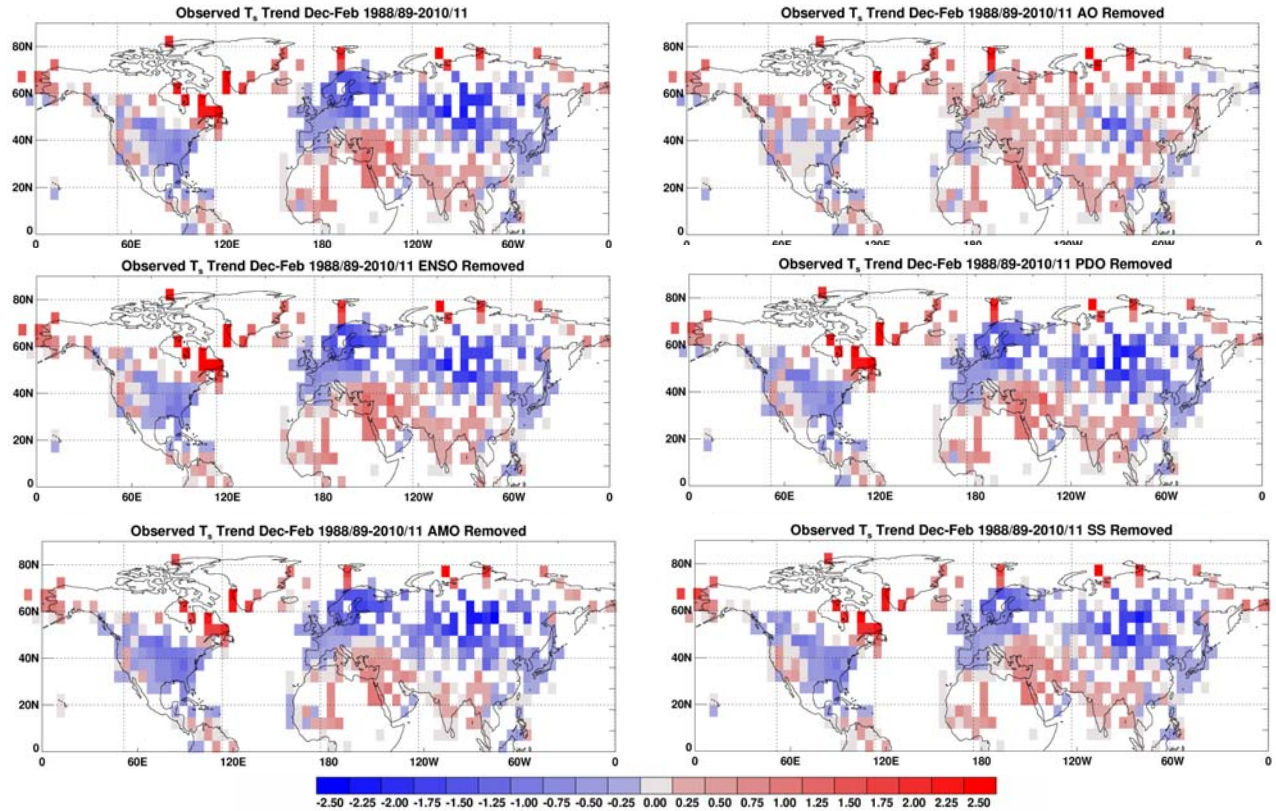
Fig. 3 a) The decadal trend in December, January, February and March land-surface temperatures 1988/89-2010-11 (top left). b) The decadal trend in December, January, February and March land-surface temperatures 1988/89-2010/11 after the regressed values of temperature with the concomitant AO have been removed (top right). c) Same as b but with ENSO removed (middle left), d) same as b but with the Pacific Decadal Oscillation removed (middle right), e) same as b but with the Atlantic Multi-Decadal Oscillation removed (bottom left) and f) same as b but with solar variability represented by sunspot number removed (bottom right). Colored shading in degrees Celsius; values between –0.25 and 0.25 are shown in grey and missing and ocean values are shown in white.

Over the past four decades, the globe has experienced continued warming. Over the past two decades this warming has continued unabated for three of the four seasons – spring, summer and fall. However, during the winter season the warming trend has all but disappeared for the extratropical NH landmasses. Large regions of the extratropical Northern Hemisphere landmasses have experienced a cooling trend, and the hemispheric temperature trend pattern closely resembles the temperature anomaly pattern associated with the negative phase of the AO.

Over the past two decades, Eurasian snow cover in October has been increasing. We argue that the positive trend in snow cover has contributed a significant fraction of the observed cooling in eastern North America and Northern Eurasia where snow cover is significantly correlated with winter temperatures (Cohen *et al.* 2009). Therefore, much of the recent observed late winter cooling across the NH is a response to increased October Siberian snow cover, increased Wave Activity Flux (WAF) mainly over Eurasia and increased stratosphere-troposphere coupling forcing a dynamical response in the hemispheric circulation. This dynamical forcing has resulted in both stratospheric polar warming and lower tropospheric cooling over the NH landmasses and has largely masked the global warming trend much more apparent earlier in the spring, summer and fall. The surface temperature trend pattern is most closely associated with the negative polarity of the AO, which has been linked with leading stratospheric circulation anomalies. We also computed how much of the winter cooling trend can be explained by the following other large-scale climate modes: the El Niño/Southern Oscillation, the Pacific Decadal Oscillation, the Atlantic Multidecadal

Oscillation and solar variability. Only the AO explains a large fraction of the observed winter cooling trend; the other climate modes explain essentially none of the observed winter cooling trend (Figure 3).

4. Conclusions

Over a decade of research has demonstrated the statistical link between October Eurasian snow cover and the phase and magnitude of the winter AO. Above we outlined a dynamical pathway beginning with the advance of snow cover in the fall and culminating with the phase of the AO and the frequency of Arctic outbreaks in the mid-latitudes. October snow cover has been used to produce skilful real-time operational winter forecasts for the extratropical NH (Cohen and Fletcher 2007).

This same pathway may also be modulating winter temperatures on a decadal scale. Though temperatures continue to rise throughout most of the year consistent with global warming, large regions of the extratropical NH have experienced winter cooling over the past two decades. An observed increasing trend in Eurasian snow cover is the most likely boundary condition for partially forcing winter hemispheric trends over the past two decades that has heretofore been identified.

References

Cohen, J., 1994: Snow cover and climate. *Weather,* **49**, 150-156.

—, and D. Rind, 1991: The effect of snow cover on the climate. *J. Climate*, **4**, 689-706.

—, and D. Entekhabi, 1999: Eurasian snow cover variability and Northern Hemisphere climate predictability. *Geophys. Res. Lett.*, **26**, 345-348.

—, and C. Fletcher, 2007: Improved Skill for Northern Hemisphere winter surface temperature predictions based on land-atmosphere fall anomalies. *J. Climate*, **20**, 4118-4132.

—, K. Saito and D. Entekhabi, 2001: The role of the Siberian high in Northern Hemisphere climate variability. *Geophys. Res. Lett.*, **28**, 299-302.

—, M. Barlow, and K. Saito, 2009: Decadal fluctuations in planetary wave forcing modulate global warming in late boreal winter. *J. Climate*, **22**, 4418–4426.

NOAA's Colorado Basin River Forecast Center: "Climate Services on the Colorado River: Capabilities, Gaps, and Chasms"

Kevin Werner

Colorado Basin River Forecast Center, Salt Lake City, UT
NOAA's National Weather Service

1. Introduction

NOAA has a long history of providing forecasts on the seasonal time scale for the Colorado River through the Colorado Basin River Forecast Center (CBRFC). As water demand has increased over recent years, so too has the thirst for information and forecasts to better inform decision-making on this scarce natural resource. This talk first described the physiogeographic and policy characteristics of the basin. Next, the current forecast services provided by the CBRFC were described including developmental activities aimed at improving those services in the future. Finally, information gaps between the current suite of services and what stakeholders are asking for were discussed. In contrast to most CTB talks, this was a non-technical talk.

2. Colorado River primer

The Colorado River drains portions of seven US states as well as portion of Mexico before it drains into the Gulf of California. In modern times, nearly the entire river has been diverted such that by the time it enters the Gulf of California, there is very little water left in the natural channel. The naturalized mean annual discharge at the Lees Ferry Gauge below Lake Powell is approximately 15.0 million acre-feet (MAF) when averaged over the past century. In contrast, the unregulated inflow to Lake Powell over the 1971-2000 period is 12.1 MAF. Approximately 85% of this runoff originates in a relatively small area above 9000 feet of elevation, where winter temperatures are cold enough that the watersheds store winter precipitation as snowpack. The strong snow accumulation and melt cycle and its variability from year to year are extremely important to both modeling and managing streamflow on the river.

Humans have been using the water resources on the Colorado since prehistoric times. However, it wasn't until the 20th century that legal frameworks began to take shape to prescribe the usage of its fresh water resources. The major governing document on the river is the 1922 Colorado Compact. This compact divided the water resources equally among the upper basin and lower basin states allocating each group 7.5 MAF per year. The geographic division between upper and lower basin states (the "compact point") was established at the river location of the Lees Ferry gauge. The Compact further allocated a maximum annual withdrawal for each state to be averaged over a
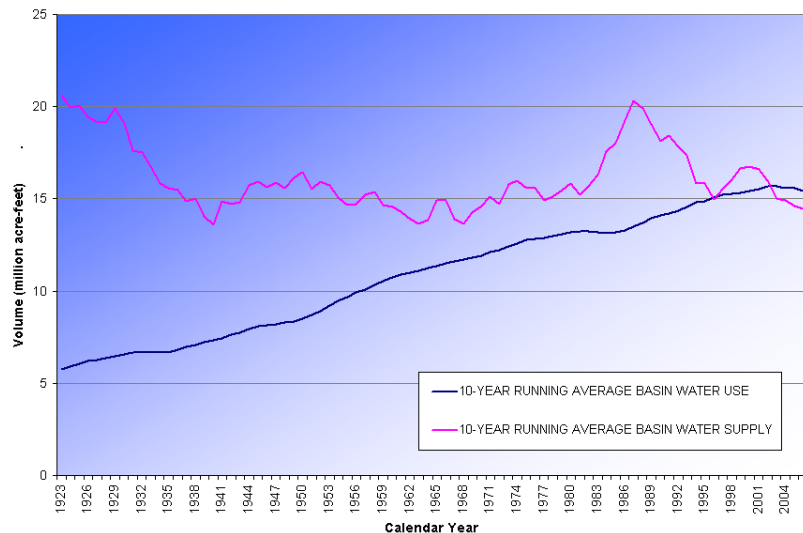

Figure 1 Long term water supply (purple) and demand (blue) for the entire Colorado Basin (USBR 2010). Note that these figures include tribuary contributions below the Lees Ferry compact point that are not included in the states' allocations.

Correspondence to: Kevin Werner, Colorado Basin River Forecast Center, NOAA/NWS, Salt Lake City, UT;
E-mail: Kevin.Werner@noaa.gov

ten year period. Subsequently, in 1944, the US and Mexico signed the Mexican Water Treaty which allocated an additional 1.5 MAF per year to Mexico, bringing the total annual allocation on the Colorado River to 16.5 MAF. As the lower basin states began to develop their water rights fully, California and Arizona entered into litigation to determine whether inflows to the river below the compact point counted as part of a state's allocation. In 1964, the US Supreme Court decided Arizona v. California, determining that inflow below the compact point is not to be counted as part of a state's allocation (1983). In practice, this meant that the 12.1 MAF

Figure 2 Lake Powell inflow (green) and forecasts (red) for 2011. Source: wateroutlook.nwrfc.noaa.gov

at the compact point has been over-allocated at 16.5 MAF. As the upper basin states have continued to develop toward their full allocations, the river has become fully used. Increased water demand coupled with reduction in water supply associated with the drought in the 2000s (Figure 1) motivated the creation of an interim operating agreement that is in place through 2026 to govern any shortages or surpluses on the system (USBR 2007).

3. Water supply forecasting for the Colorado

The CBRFC has been issuing seasonal water supply forecasts on the Colorado River for over seven decades. These forecasts predict the volume of the spring runoff at many locations important to water management throughout the basin. Since the 1970s, these forecasts have been coordinated with the USDA/NRCS National Water and Climate Center. Figure 2 shows an example of the forecasts for Lake Powell inflow in 2011. The major source of forecast skill (runoff predictability) is the snowpack on the ground at the time of the forecast issuance, though soil moisture plays a lesser role in predictability. Many studies and years of experience have shown that in the upper Colorado River basin, climate predictability associated with the El Nino Southern Oscillation (ENSO) is weak. Figure 3 shows the correlation between upper Colorado water supply streamflow volume and the concurrent Nino 3.4 index of the ENSO phenomenon.

Forecasts are generated through two primary methods at the CBRFC – statistical and dynamical. Statistical prediction relies on equations that relate predictors – typically snow water readings at snow courses or SNOTELs, accumulated water year precipitation measured at NWS Cooperative Observer stations, and occasionally observed streamflow – and the predictand, the runoff volume at the forecast point. Both the CBRFC and the USDA/NRCS National Water and Climate Center use a similar form of statistical forecasting called principal components regression (Garen, 1992). The technique is applicable to the incorporation of climate forecasts, but due to their weak skill, such forecasts are not used in practice. At CBRFC, statistical prediction is only used for once-monthly predictions between January and June, when the snow predictors have significant values.
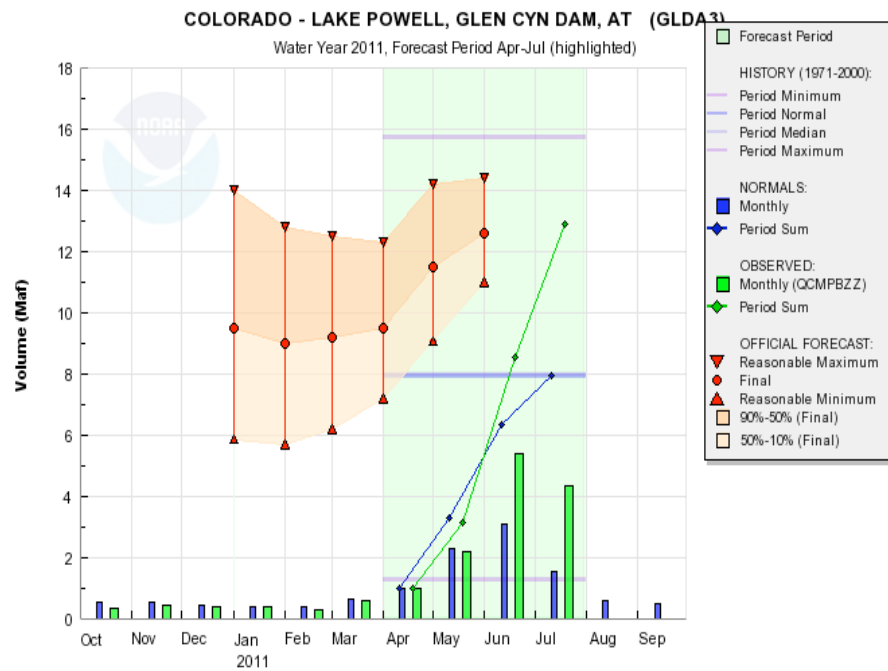
The second water supply prediction method employed by CBRFC is ensemble streamflow prediction (ESP). ESP makes use of the hydrologic simulation model that is also used for daily streamflow prediction operations to support flood warning and short term reservoir management. CBRFC uses the Sacramento Soil Moisture Accounting Model (Sac-SMA; (Burnash and Ferral 1973)) and the SNOW-17 temperature index model (Anderson 1973). Each of these models is calibrated to simulate observed streamflow over a 30 year historical period (1981-2010). The temperature and precipitation time series inputs to the models from this calibration period are used as a climate forecast ensemble inputs to

Figure 3   Lake Powell April-July inflow vs January-March Nino3.4 index (NWS 2011).

generate a forecast ensemble of streamflow. Forecasts start from the simulation model variable states (e.g., snow water equivalent, soil moisture) that reflect the current conditions in the basin's watersheds (Day 1985). ESP forecasts may be updated at any frequency.
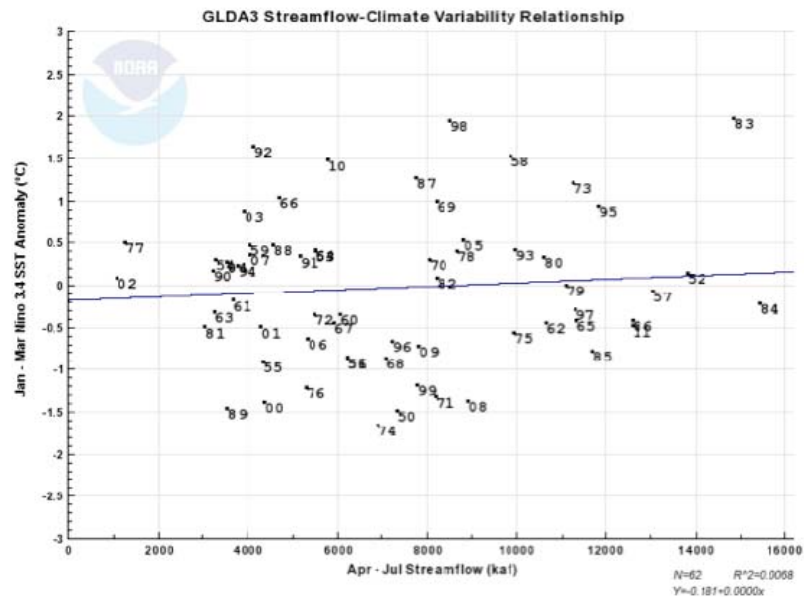
Forecasts are currently used by users such as the US Bureau of Reclamation (hereafter Reclamation), Denver Water and PacifiCorps (water and energy utilities) as input to reservoir operations management and planning models. Reclamation uses the "24-month study" model, which as the name suggests, helps plan monthly reservoir releases 2 years into the future using a combination of ESP and official water supply forecasts. This model is run once per month but only three times per year using the 10th and 90th percentile forecasted monthly runoff volumes. Stakeholders have expressed concerns that the projections from this model, particularly in the 2nd year of the forecast, have low skill, and observed that the 10th-90th percentile outputs to bracket a range of uncertainty does not provide sufficient probabilistic information to support risk-based decision making in their own resource management activities that depend on Colorado River water allocations.

4. The future: progress and challenges

Stakeholder demand for increased information and forecasts has led both CBRFC and Reclamation to undertake major research and development initiatives to improve forecasts and information available to stakeholders. CBRFC has launched a seasonal to year-two forecast intercomparison effort that is supported by collaborative research with academic partners who are assessing methods for statistical climate and flow prediction, and workshops to bring together stakeholders, researchers and forecasters, and a water-management oriented testbed to focus intercomparison efforts on streamflow predictions that have the most impact on Colorado River management. CBRFC has also implemented an ensemble forecast technique developed at the NWS Office of Hydrologic Development to create meteorological forecast ensemble (hence streamflow ensembles) based on weather and climate variable outputs from global numerical weather and climate prediction models. This meteorological forecasting technique is similar to a technique developed at CBRFC in the early 2000s (Werner, Brandon *et al.* 2005). It is also a centerpiece of the nascent NWS Hydrologic Ensemble Forecast Service (HEFS), and is described in Schaake *et al.* (2007) and Wu *et al.* (2011). CBRFC began running this technique in an experimental mode in 2010. Figure 4 shows an example of this ensemble forecast for Lake Powell inflow.

At the same time, Reclamation has invested in upgrading their modeling system from the 24-month study to the Mid-Term Operations Model (MTOM). MTOM is an objective, ensemble based operations model used for planning reservoir operations in an ensemble (probabilistic) mode. It is based on a 24 month long ESP forecast for monthly inflow volumes to the major Reclamation reservoirs in the Colorado Basin. MTOM began running in an experimental mode in 2010, in parallel its current operations.

The new collaborative activities, forecast inter-comparison testbeds and forecasting and operations models at CBRFC and Reclamation present possibilities for addressing both long standing and more recent

Figure 4 Example of ensemble streamflow forecasts for Lake Powell inflow based on ensemble weather and climate predictions (CBRFC 2011).

stakeholder requirements. Foremost among these is the new incorporation of climate predictions out to two years (ultimately out to five years) as input to the CBRFC streamflow forecast system. The large storage to annual flow ratio (approximately 4:1) and the high economic value of Colorado River water resources implies great potential for benefit from seasonal climate forecasts even if there is minimal skill in the climate predictions. Given the very low correlation between Lake Powell inflow and ENSO (*e.g.* Figure 3), developing skillfull climate forecasts for this region is difficult.

Both the science and stakeholder communities have inquired about or articulated other areas for attention that could lead to improvements in streamflow forecasting in the Colorado Basin. These include:

- The 'dust-on-snow' phenomenon, which has shown large inter-annual variability (*e.g.* Painter, Barrett *et al.* 2007) and influences snow-melt timing and potentially magnitude.
- Beetle kill of various species of pine forests, which has affected major swaths of land area in the Rocky Mountains.
- Reliable ensemble climate and streamflow forecasts on time scales from hours to years
- Water demand and evapotranspiration forecasts and analysis
- Improved stakeholder interactions to match forecast and information needs with stakeholder operational requirements
- A transition toward more transparent and objective methods for streamflow prediction
- An upgrade of NWS hydrologic prediction systems from the legacy NWS River Forecast System to a new state-of-the-art platform called the Community Hydrologic Prediction System (CHPS), designed to facilitate collaboration and partnerships and greater flexibility in forecasting approaches.

Ultimately, NOAA's mission "to understand and predict changes in the Earth's environment … to meet our Nation's economic, social, and environmental needs" (NOAA 2009) should guide both science and service activities to meet the needs of the various water resources stakeholders in the Colorado basin. Accordingly, the CBRFC has recently begun to play an active if not central role in spurring the development of new and improved scientific and operational approaches that support this mission. These have come in the form of internal research and development efforts as well as the forging of partnerships with external research and
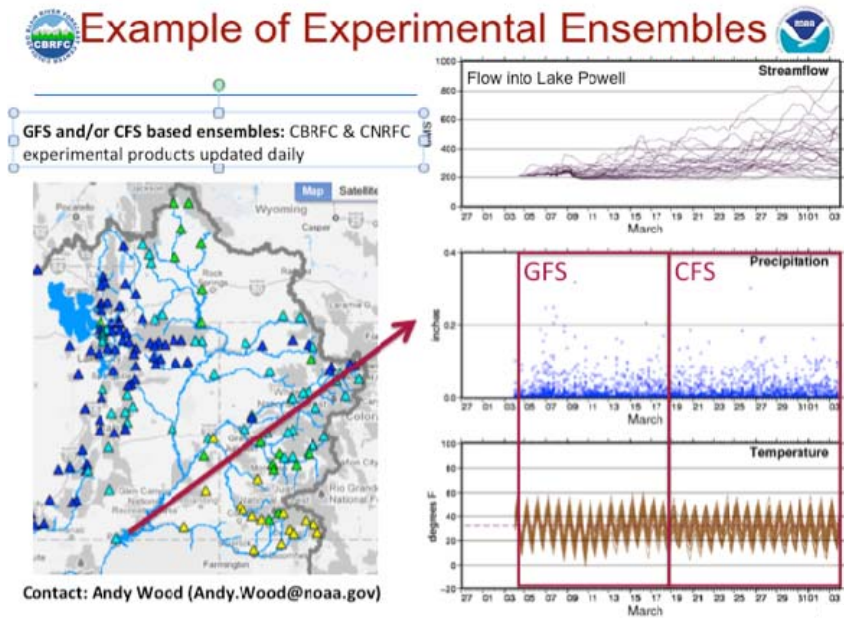
operations groups both in NOAA, in water management agencies, in academia, and in stakeholder communities. Though many of these activities are still in early phases, they hold great potential to deliver a significant improvements in the quality of CBRFC's hydrologic predictions and associated benefits for stakeholders and the nation.

References

Anderson, E.A., 1973: National Weather Service river forecast system--snow accumulation and ablation model. *TECHNICAL MEMORANDUM NWS HYDRO-17*, November 1973. 217 P.

Burnash, R.J.C. and R. Ferral, 1973: Generalized hydrologic modeling, a key to drought analysis. *IN: FLOODS AND DROUGHTS*.

CBRFC, 2011: CBRFC Hydrologic Ensemble Forecast System. Retrieved August 23, 2011, from http://www.cbrfc.noaa.gov/devel/hefs/.

Day, G.N., 1985: Extended streamflow forecasting using NWSRFS. *Journal of Water Resources Planning and Management,* **111**, 157-170.

NOAA, 2009: About NOAA. Retrieved August 31, 2007, from http://www.noaa.gov/about-noaa.html.

NWS, 2011: National Water Resources Outlook. Retrieved August 23, 2011, from http://wateroutlook.nwrfc.noaa.gov.

Painter, T.H., A.P. Barrett, and co-authors, 2007: Impact of disturbed desert soils on duration of mountain snow cover. *Geophys. Res. Lett*, **34**, 1-6.

Schaake, J., J. Demargne, and co-authors, 2007: Precipitation and temperature ensemble forecasts from single-value forecasts. *Hydrology and Earth System Sciences Discussions*, **4**, 655-717.

USBR, 2007: Record of Decision: Colorado River Interim Guidelines for Lower Basin Shortages and the Coordinated Operations for Lake Powell and Lake Mead. U. S. Bureau of Reclamation, Department of Interior.

—, 2010: Colorado River Supply and Demand. U. S. Bureau of Reclamation, Department of Interior.

U.S. Supreme Court, 1983: Arizona v. California. 460 U.S. 605.

Werner, K., D. Brandon, and co-aothors, 2005: Incorporating medium-range numerical weather model output into the ensemble streamflow prediction system of the National Weather Service. *Journal of Hydrometeorology*, **6**, 101-114.

Wu, L., D. J. Seo, and co-authors, 2011: Generation of ensemble precipitation forecast from single-valued quantitative precipitation forecast for hydrologic ensemble prediction. *Journal of Hydrology*.

CFS – Stratosphere Improvement

Judith Perlwitz[1], Jordan Alpert[2], Amy Butler[3], Craig Long[3], Shuntai Zhou[3], Tao Zhang[1]

[1]CIRES, University of Colorado, and NOAA/ESRL Physical Sciences Division, Boulder, Colorado
[2]NOAA/NCEP Environmental Modeling Center, Camp Springs, Maryland
[3]NOAA/NCEP Climate Prediction Center, Camp Springs, Maryland

1. Introduction

Troposphere and stratospheric are closely coupled dynamically with the tropospheric impact on the stratosphere dominating. However, the stratosphere provides an important pathway by which tropospheric circulation anomalies can be modified. Degrading the representation of stratospheric processes in atmospheric general circulation models has important implications for modeling the tropospheric climate state, its variability and its sensitivity to external forcing. A recent "Assessment of Intraseasonal to Interannual (ISI) Climate Prediction and Predictability" (National Research Council, 2010) recommended that operational ISI prediction models should be improved to represent stratosphere-troposphere interactions.

The main goal of this Climate Test Bed project is to improve the representation of stratospheric processes in the Climate Forecast System (CFS). Because the CFS version 2 was not available during the first year of the project, we worked with interims versions of the CFS and (1) evaluated troposphere-stratosphere coupling in the atmospheric component of the CFS, and (2) investigated the sensitivity of the CFS to orographic gravity wave drag parameterization.
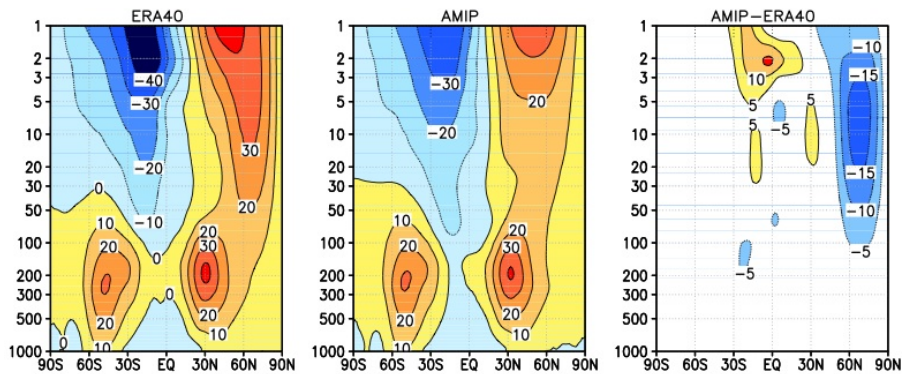

Fig. 1 Dec-Feb average of zonal mean zonal wind [m/s] for ERA40 (left), GFSCFS AMIP simulation middle and their difference (AMIP minus ERA40).

2. Results

(a) Evaluation of troposphere-stratosphere coupling

We carried out an AMIP simulation based on the atmospheric component of the CFS (GFS$_{CFS}$). In this simulation, the observed evolution of sea surface temperatures and sea ice concentration from 1970 to 2008 is described as lower boundary forcing. The data are evaluated based on ERA-40 reanalysis. We first investigated the stratospheric basic state. We found that during December-February, the polar night jet in the Northern Hemisphere is too weak by up to 15 m/s (Figure 1). While the model is capable of simulating major stratospheric sudden warmings, it is not able to simulate strong polar vortex events in the stratosphere (not shown). Consistent with this bias, the model climatology of 500 hPa heights is shifted towards a negative North Atlantic Oscillation phase relative to ERA40 (Figure 2).
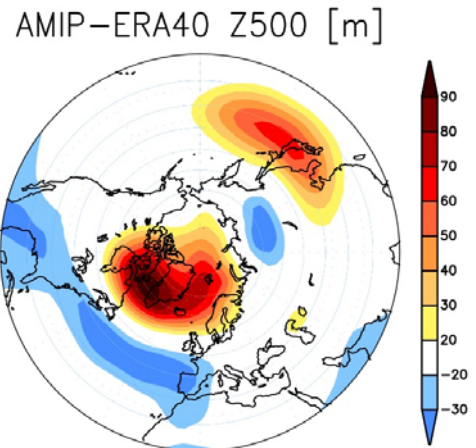

Fig. 2 Dec-Feb mean 500 hPa (bottom) height differences [m] between the GFS$_{CFS}$ AMIP simulations and ERA40 reanalysis .

_____

We investigated the troposphere-stratosphere coupling on intra-seasonal time scale using the diagnostics applied in Shaw *et al.* (2010) to ERA40 reanalysis. We distinguish between downward wave coupling, which occurs when planetary waves reflected in the stratosphere impact the troposphere, and zonal-mean coupling, which results from wave dissipation and its subsequent impact on the zonal-mean flow.

In the Northern Hemisphere (Figure 3 right panels), downward zonal mean coupling is not well represented in the GFS$_{CFS}$ (shading). While in ERA40 there is a clear shift of the correlation of the 20 hPa Northern Hemisphere Annular Mode (NAM) index with the near surface NAM index towards positive time lags, in the GFS$_{CFS}$ maximum correlations are found around lag zero with little persistence towards positive lags. In addition, the model does not simulate downward wave coupling. ERA40 shows a significant relationship of wave 1 in the stratosphere with wave 1 in the troposphere at positive lags indicative of an impact of the stratosphere on the troposphere (solid lines). In the model, such an impact is not found. This is related to the fact that the model is not able to simulate a reflective configuration of the stratospheric basic state in the boreal winter hemisphere (not shown). In the Southern Hemisphere (Figure 3, left panels), the model simulates well the downward wave coupling as indicated by wave 1 correlations at positive lags (isolines). Zonal mean downward coupling is larger in the model than in ERA40. In the Southern Hemisphere this coupling is more instantaneous.

Fig. 3 Lag-height sections of correlations between daily stratospheric and tropospheric circulation in the extratropical Northern and Southern Hemisphere with the 20hPa level as reference level. Shown are correlations of annular mode (zonal mean coupling, shaded), and wave 1 cross correlation (isolines) during active season of dynamical troposphere-stratosphere coupling. (Top) ERA40 and (bottom) GFS$_{CFS}$ AMIP simulation.

(b) Model sensitivity to orographic gravity wave drag parameterization

We carried out two sets of twin experiments with the CFS. One set was carried out for the La Niña winter 2007/08 and the other was carried out for the El Niño winter 2009/2010. A twin experiment ensemble consists of a control simulation with the CFS and an experiment in which the orographic gravity wave drag (GWD) was increased by a factor of four to determine the sensitivity of the stratosphere in the CFS to the strength of the orographic gravity wave drag parameterization. Each ensemble is based on 6 individual runs starting at different initial conditions. Figures 4 and 5 show the Dec-Feb zonal mean zonal wind anomalies relative to NCEP/DOE R2 reanalysis. The results indicate that the increased orographic GWD increases biases in the Northern Hemisphere stratospheric basic state.

3. Conclusion

The results indicate that the model is biased to a weak stratospheric polar winter vortex with subsequent effects on the tropospheric circulation especially over the North Atlantic region. These biases are accompanied by strongly reduced downward stratosphere-troposphere coupling on intra-seasonal time scale. These biases are consistent with the observed relationship between the strength of the stratospheric polar
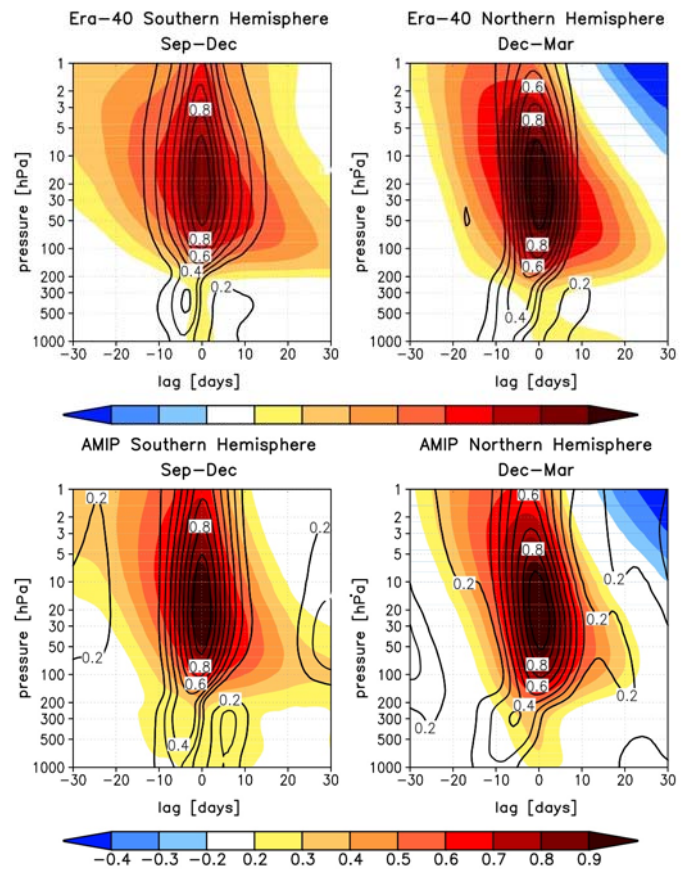
winter vortex and westerlies over the North Atlantic region (*e.g.*, Perlwitz and Graf, 1995), and are related to the degraded stratospheric representation in the model (*e.g.*, Boville, 1984). The biases increase further in the case of increased orographic GWD.

    To improve the representation of the troposphere-stratosphere coupling in the model, we plan to raise the model lid from 0.2 to 0.006 hPa, increase the number of layers from 64 to 91, and incorporate a non-orographic gravity wave drag parameterization.

References

Boville, Byron A., 1984: The Influence of the Polar Night Jet on the Tropospheric Circulation in a GCM. *J. Atmos. Sci.*, **41**, 1132–1142.

National Research Council, National Academies, 2010: Assessment of Intraseasonal to Interannual Climate Prediction and Predictability. *The National Academies Press*, 192pp.

Perlwitz, J., and H.-F. Graf, 1995: The statistical connection between tropospheric and stratospheric circulation of the Northern Hemisphere in winter. *J. Climate,* **8**, 2281-2295.

Shaw, T. A., J. Perlwitz and N. Harnik, 2010: Downward wave coupling between the stratosphere and troposphere: the importance of meridional wave guiding and comparison with zonal-mean coupling. *J. Climate,* in press.

Fig. 4 DJF ensemble difference of zonal mean zonal wind between CFS simulation and NCEP/DOE (R2) reanalysis for year 2009/2010. (Left) control and (right) increased GWD.
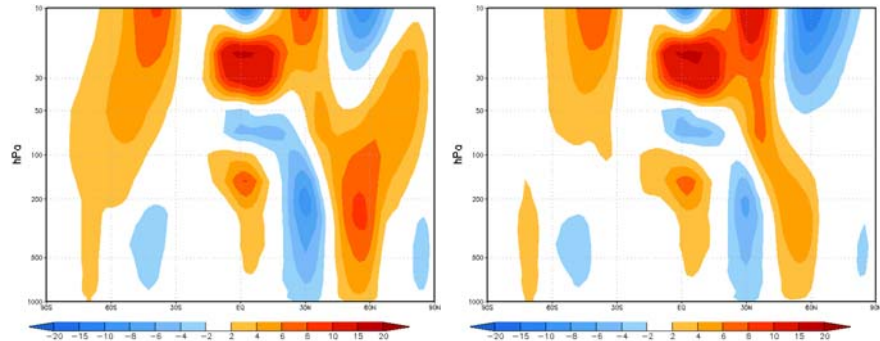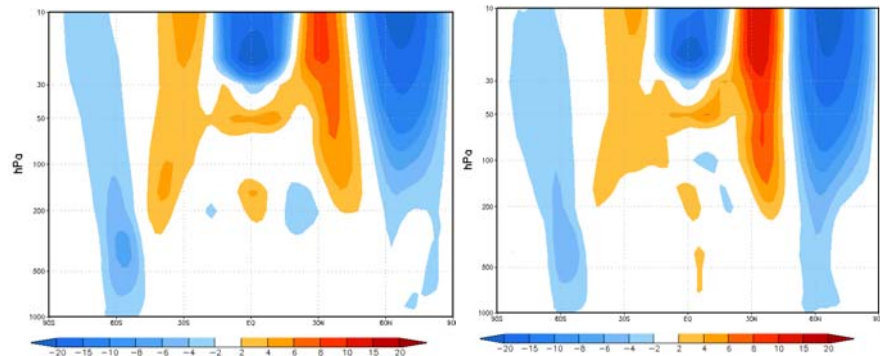

Fig. 5 DJF ensemble difference of zonal mean zonal wind between CFS simulation and NCEP/DOE (R2) reanalysis for year 2007/2008. (Left) control and (right) increased GWD.

The GEOS-5 AOGCM

Yury Vikhliaev, Max Suarez, Michele Rienecker, Jelena Marshak, Bin Zhao,
Robin Kovack, Yehui Chang, Jossy Jacob, Larry Takacs, Andrea Molod, Siegfried Schubert

Global Modeling and Assimilation Office, NASA/Goddard Space Flight Center, Greenbelt, Maryland

1. Introduction

The GEOS-5 Atmosphere-Ocean General Circulation Model (AOGCM) is a state-of-the art coupled climate model developed at the Global Modeling and Assimilation Office (GMAO). In this presentation, an overview of the model design is given, and model performance is evaluated in terms of simulating the mean climate and inter-annual climate variability.

The GEOS-5 AOGCM is designed to simulate climate variability on a wide range of time scales, from synoptic time scales to multi-century climate change, and have been tested in coupled simulations and data assimilation mode.

The main components of the GEOS-5 AOGCM (Fig. 1) are the atmospheric model, the catchment land surface model, both developed by the GMAO (GEOS-5 AGCM, Rienecker *et al.* 2008), and MOM4, the ocean model developed by the Geophysical Fluid Dynamics Laboratory (Griffies *et al.* 2005). These two components exchange fluxes of momentum, heat and fresh water through a "skin layer" interface. The skin layer includes

Fig. 1 Components of the GEOS-5 AOGCM. Components in the black frame are used in a production of AGCM data assimilation system. Other components are tested in coupled and data assimilation modes.

parameterization of the diurnal cycle and a sea ice model (LANL CICE, Hunke and Lipscomb 2008). All components are coupled together using the Earth System Modeling Framework (ESMF) interface.
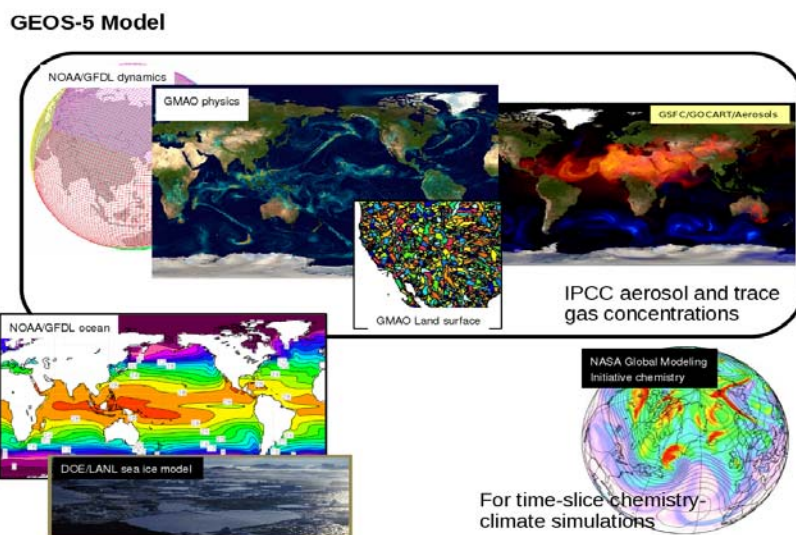
2. Experiment design

A 150-year validation experiment has been conducted to test the current performance of the GEOS-5 AOGCM. The resolution of the atmospheric component in this experiment is 2.5° longitude × 2° latitude with 72 vertical levels up to 0.01hPa. The ocean resolution is 1° longitude and latitude, with meridional equatorial refinement to 1/3°, and 50 vertical levels. A coupled model configuration with a 1.5°×1° atmospheric grid, and 0.5° ocean grid is also being tested. Initial conditions for the atmospheric component are taken from an uncoupled experiment forced by the observed sea surface temperature. The ocean is initialized with a steady state, with temperature and salinity from the Levitus and Boyer climatology. The atmospheric state in the coupled experiment is compared to the results from an uncoupled experiment and also MERRA. This analysis allows us to understand which errors can be attributed to coupling and which errors result from deficiencies in the AGCM. The ocean state is validated using observations and the fields from the GMAO ocean data assimilation system.

_____

Correspondence to: Yury Vikhliaev, Global Modeling and Assimilation Office, NASA/Goddard Space Flight Center, Greenbelt, Maryland; E-mail: yury.v.Vikhliaev@nasa.gov

The idea to have a multi-scale modeling system with unified physics is to be able to propagate improvements made to a physical process in one component into the other the components smoothly and efficiently. In addition, this model system has been coupled to a *Satellite Data Simulation Unit* that can compute satellite-consistent radiances or backscattering signals from simulated atmospheric profiles and condensates consistent with the unified microphysics within the multi-scale modeling system (Fig. 1).

3. Results

The 150-year integration produced a stable, realistic mean climate and inter-annual climate variability. The key features of climate simulated by the model are summarized below.

The mean atmospheric state simulated by the AOGCM is similar to atmospheric state simulated by the GEOS5 AGCM forced by the observed sea surface temperature (SST). Errors in the coupled simulation primarily have the same structure as errors in the uncoupled simulation, but usually with larger magnitude. These errors include: too strong surface wind stress in high

Fig. 2 Sea surface temperature (top) from the GEOS-5 coupled integration, and the bias relative to the Reynolds climatology (bottom).

latitudes; too strong cloud radiative forcing in low latitudes, and too weak cloud radiative forcing in high latitudes; errors in precipitation typical of most state-of-the-art climate models, *e.g.*, a strong double Inter-Tropical Convergence Zone (ITCZ).

On the ocean side, the upper ocean circulation and surface climate reach equilibrium in several decades, while the deep ocean circulation still exhibits a drift after 150 years of integration. SST is an important measure of the realism of the model climate, since it is used by the atmospheric component as a boundary condition. Figure 2 shows that the model SST simulation is quite realistic. The dominant errors shown in Figure 2 are typical for state-of-the-art climate models. For example, the warm SST bias near the eastern boundaries of the oceans is due to deficiencies in simulating the orientation of the wind stress and the coastal upwelling. SST errors in the regions of western boundary currents result from deficiencies in simulating the strength of the western boundary currents and the separation location. These types of errors are typically reduced with the increased resolution.

The leading mode of global SST variability is shown in Figure 3. This mode exhibits the prominent El Nino - Southern Oscillation pattern which varies on inter-annual time scales. Compared to observations, the model El Nino pattern is narrower and extended further into the western Pacific. In addition to the dominant signal in the equatorial Pacific, the model also captures the co-variability in the sub-tropical Pacific. Comparison between the model and observed time series of the leading SST mode shows that model ENSO has reasonable time scale and irregularity with a tendency to have slightly higher frequency than observed. Analysis of correlation between ENSO time series and 300mb geopotential height (not shown) demonstrates that the model simulates realistic tropical-extratropical ENSO teleconnections.
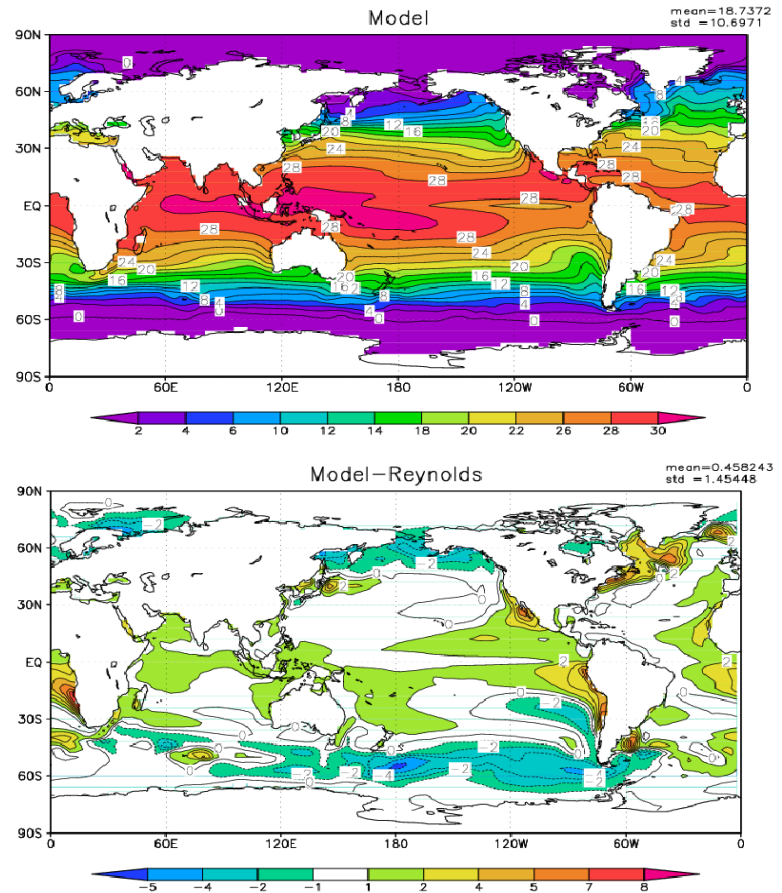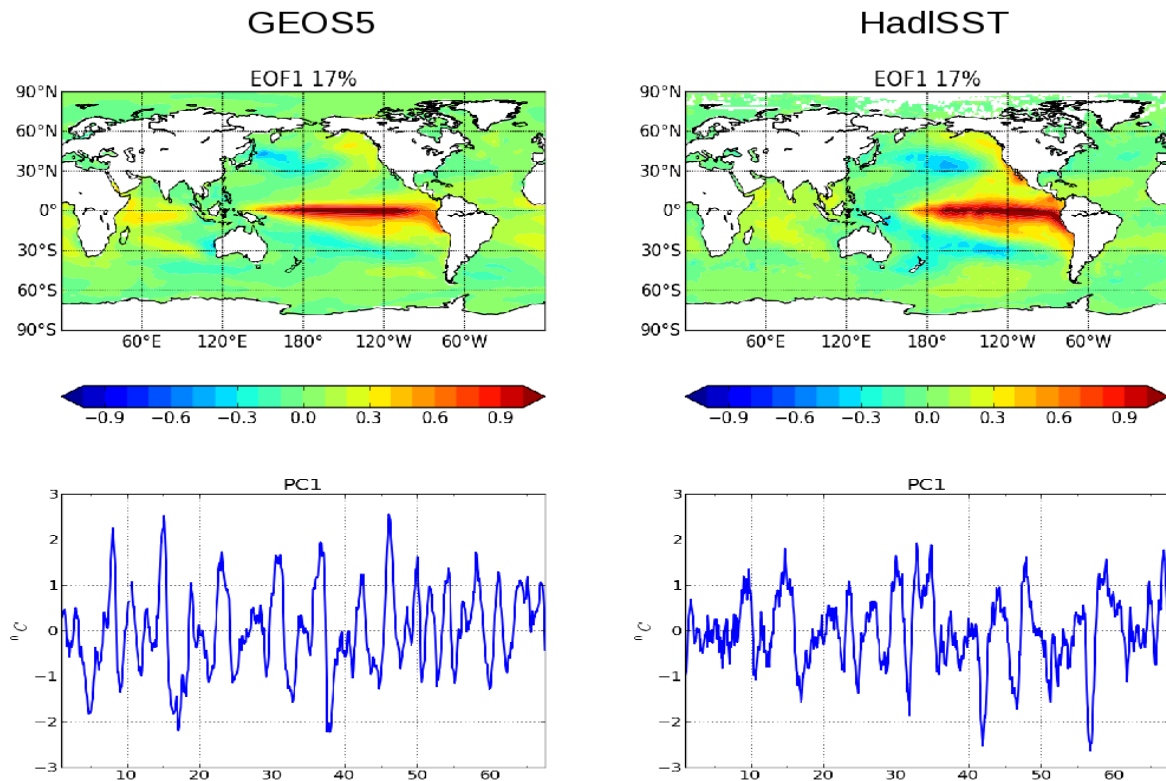
Fig. 3 The leading mode of global SST variability from the GEOS-5 AOGCM (left) and the Hadley center (right). Top panels show the leading empirical orthogonal functions of the global SST. Bottom panels show corresponding principal components.

4. Conclusions

Development of the GEOS-5 AOGCM is a significant advance in NASA's climate modeling. Current performance of the model is comparable to performance of the state-of-the art coupled climate models being used for the next IPCC assesment report. The model now routinely runs on the supercomputing clusters at the NASA Center for Climate Simulation (NCCS) and the NASA Advanced Supercomputing Division (NAS). Projects underway with the GEOS-5 AOGCM include weakly coupled ocean-atmosphere data assimilation, seasonal climate predictions and decadal climate prediction tests within the framework of Coupled Model Intercomparison Project Phase 5 (Program for Climate Model Diagnosis and Intercomparison). The decadal climate prediction experiments are being initialized using the weakly coupled atmosphere-ocean data assimilation based on MERRA. The results of these experiments will be distributed through the NCCS Earth Grid System node.

References

Rienecker, M. M., and Coauthors, 2008: The GEOS-5 Data Assimilation System - Documentation of Versions 5.0.1, 5.1.0, and 5.2.0, Technical Report Series on Global Modeling and Data Assimilation, NASA/GMAO.

Griffies, S. M., and Coauthors, 2005: Formulation of an ocean model for global climate simulations. Ocean Science, 45-79.

Hunke, E. C., and W. H. Lipscomb, 2008: CICE: The Los Alamos Sea Ice Model, Documentation and Software Manual, Version 4.0. Techniocal Report, Los Alamos National Laboratory.

Program for Climate Model Diagnosis and Intercomparison: CMIP5 - Coupled Model Intercomparison Project Phase 5 - Overview, http://cmip-pcmdi.llnl.gov/cmip5/index.html?submenuheader=0

The Goddard Multi-Scale Modeling System with Unified Physics

W.-K. Tao[1], J. Chern[1,2], T. Iguchi[1,3], S. Lang[1,4], C. Peters-Lidard[5], X. Li[1,2],
T. Matsui[1,3], K. Mohr[1], B.-W. Shen[1,3], J. J. Shi[1,2], and X. Zeng[1,2]

[1]*Laboratory for Atmospheres, NASA/Goddard Space Flight Center, Greenbelt, Maryland*
[2]*Goddard Earth Sciences and Technology Center, University of Maryland, Baltimore County, Maryland*
[3]*Earth System Science Interdisciplinary Center, University of Maryland, College Park, Maryland*
[4]*Science Systems and Applications Inc., Greenbelt, Maryland*
[5]*Laboratory for Hydrospheric Processes, NASA/Goddard Space Flight Center, Greenbelt, Maryland*

1. Introduction

The foremost challenge in parameterizing subgrid convective clouds and cloud systems in large-scale models is the many coupled physical processes (*i.e.*, radiation and surface processes) that interact over a wide range of scales, from microphysical scales to the meso-scale. This makes the comprehension and representation of convective clouds and cloud systems one of the most complex scientific problems in earth science. On one hand, clouds and cloud systems owe their origin to large-scale dynamic and thermodynamic forcing, radiative cooling in the atmosphere, and turbulent transfer processes at the surface (*e.g.*, the transfer of heat and moisture from the ocean to the atmosphere). On the other hand, clouds and cloud systems serve
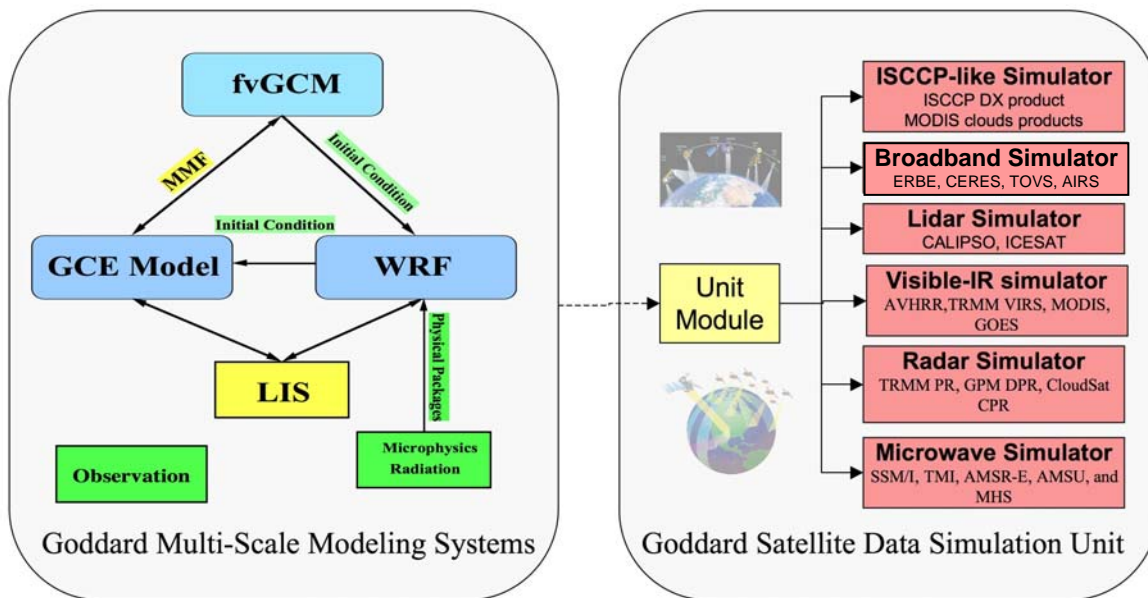

Fig. 1 Schematic diagram of the Goddard Multi-scale Modeling System with unified physics coupled with the Goddard Satellite Data Simulation Unit (SDSU). The coupling between the fvGCM and GCE is two-way [termed a multi-scale modeling framework (MMF)], while the coupling between the fvGCM and WRF and WRF and the GCE is only one-way. LIS is the Land Information System developed in the Goddard Hydrological Sciences Branch. LIS has been coupled interactively with both WRF and the GCE. Additionally, WRF has been enhanced by the addition of several of the GCE model's physical packages (i.e., microphysical scheme with four different options and short and long-wave radiative transfer processes with explicit cloud-radiation interactive processes). Observations (obtained from satellite and ground-based campaigns) play a very important role in providing data sets for model initialization and validation and consequently improvements. The Goddard SDSU can convert the simulated cloud and atmospheric quantities into radiance and backscattering signals consistent with those observed from NASA EOS satellites.

_____

Correspondence to: W.-K. Tao, Laboratory for Atmospheres, NASA/Goddard Space Flight Center, Greenbelt, Maryland; E-mail: wei-kuo.tao-1@nasa.gov

as important mechanisms for the vertical redistribution of momentum, trace gases (including the greenhouse gas, CO2), aerosols, and sensible and latent heat on the large-scale. It is also generally accepted that the proper representation of physical cloud processes in GCMs (general circulation models) is vital to advancing their predictive skill of the water and energy cycles.

As such, the highest science priority identified in the Global Change Research Program (GCRP) is the role of clouds and their interaction with radiation in climate and hydrological systems. For this reason, the Global Energy and Water Cycle Experiment (GEWEX) formed the GEWEX Cloud System Study (GCSS) to address such problems. Cloud ensemble models [CEMs, also called cloud-resolving models (CRMs) or cloud-system resolving models (CSRMs)] were identified as the primary means for carrying out these studies. CRMs now provide statistical information useful for developing more realistic statistics- or physics-based parameterizations for climate models. A CRM, typically, is not a global model and can only simulate cloud ensembles over a relatively small domain (*i.e.*, 500-1000 x 500-1000 km^2). To better represent convective clouds and cloud systems in large-scale models, a GCM coupled with CRMs (termed a *super-parameterization* or *multi-scale modeling framework, MMF*) is required given the feasible computational power. The use of a GCM enables global coverage, while the CRMs allow for better and more sophisticated physical parameterizations (*i.e.*, CRM-based physics). In addition, the MMF can utilize current and future satellite programs that provide cloud, precipitation, aerosol and other data at very fine spatial and temporal scales over the entire globe.

Type of Model (Spatial Scale)	Strengths	Weaknesses
GCMs (10^2 km)	Global Coverage Climate Change Assessment	Coarse Resolution Cumulus Parameterization
Regional Scale Models (10^1 - 10^0 km)	Regional Coverage – Regional Climate Better parameterization (nesting technology)	No Feedback to Global Circulation Case Study
Cloud Resolving Models (10^0 – 10^{-1} km)	Better physics Better Treatment of Cloud-Radiation Interaction	Small Domain No Feedback to Global Circulation Case Study (Field Campaign)
Coupled GCM-CRM (MMF) (10^2 – 4 km)	Global Coverage CRM-Based Physics	Computational Cost 2D CRM Embedded (4 km grid)
Global Cloud Resolving Model (0^0 km)	Global Coverage CRM-Based Physics	Computational Cost Data Management/Analyses

Table 1 A brief summary of the strengths and weaknesses of different modeling approaches

The traditional CRM, however, needs large-scale advective forcing in temperature and water vapor from intensive sounding networks deployed during major field experiments or from large-scale model analyses to be imposed as an external forcing. The advantage of this approach is that the simulated rainfall, temperature and water vapor budget are forced to be in good agreement with observations (see Tao and Moncrieff 2003; Tao 2003, 2007 for review). But, there is no feedback from the CRM to the large-scale model (*i.e.*, the CRM environment). In contrast, an MMF allows explicit interactions between the CRM and the GCM. With the traditional approach, CRMs can only examine the sensitivity of model grid size or physics for one type of cloud/cloud system at a single geographic location. MMFs, however, could be used to identify the optimal grid size and physical processes (*i.e.*, microphysics, cloud-radiation interaction) on a global scale. For example, MMFs can be used to identify the optimal grid size and physical processes (*i.e.*, microphysics, cloud-radiation interactions) needed for non-hydrostatic global CRMs (Satoh *et al.* 2005; Nasuno *et al.* 2008[1]).

---

[1] This model is intended for high-resolution climate simulations and has been performed on an aqua planet setup with grid intervals of 7 and 3.5 km for seasonal simulation (due its extensive computation requirement and data storage).

Regional forecast models (*i.e.*, the Weather Research and Forecasting Model or WRF) can also be conducted in CRM mode and could cover large domains (*i.e.*, a tropical channel model) through a two-way interactive nesting technique. The physical processes developed/tested for CRMs could be also used for regional scale models from idealized research to operational forecasting. It is expected that a close collaboration between CRMs, regional scale models, MMFs and non-hydrostatic high-resolution regional and global cloud resolving models can enhance our ability to simulate realistic weather and climate in the near future. The strengths and weaknesses of different modeling approaches are summarized in Table 1.

2. The Goddard Multi-Scale Modeling System

Recently, a multi-scale modeling system with unified physics was developed at NASA Goddard. It consists of (1) the Goddard Cumulus Ensemble model (GCE), a cloud-resolving model (CRM), (2) the NASA unified Weather Research and Forecasting Model (WRF), a region-scale model, and (3) the coupled fvGCM-GCE, the GCE coupled to a general circulation model (MMF). The same cloud microphysical processes, long- and short-wave radiative transfer and land-surface processes are applied in all of the models to study explicit cloud-radiation and cloud-surface interactive processes in this multi-scale modeling system. This modeling system has been coupled with a multi-satellite simulator for comparison and validation with NASA high-resolution satellite data. Figure 1 shows the multi-scale modeling system with unified physics. The GCE and WRF share the same microphysical and radiative transfer processes (including the cloud-interaction) and land information system (LIS). The same GCE physics will also be utilized in the Goddard MMF.

The idea to have a multi-scale modeling system with unified physics is to be able to propagate improvements made to a physical process in one component into the other the components smoothly and efficiently. In addition, this model system has been coupled to a *Satellite Data Simulation Unit* that can compute satellite-consistent radiances or backscattering signals from simulated atmospheric profiles and condensates consistent with the unified microphysics within the multi-scale modeling system (Fig. 1).

Parameters/Processes	GCE Model
Dynamics	Anelastic or Compressible 2D (Slab- and Axis-symmetric) and 3D
Vertical Coordinate	Z (height)
Microphysics	2-Class Water & 3-Class Ice 2-Class Water & 2-Moment 4-Class Ice Spectral-Bin Microphysics
Numerical Methods	Positive Definite Advection for Scalar Variables; 4th-Order for Dynamic Variables
Initialization	Initial Conditions with Forcing from Observations/Large-Scale Models
FDDA	Nudging
Radiation	k-Distribution and Four-Stream Discrete-Ordinate Scattering (8 bands) Explicit Cloud-Radiation Interaction
Sub-Grid Diffusion	TKE (1.5 order)
Surface Energy Budget	Force-Restore Method 7-Layer Soil Model (PLACE), Land Information System (LIS) TOGA COARE Flux Module
Parallelization	OPEN-MP and MPI

Table 2 Major characteristics of the Goddard Cumulus Ensemble (GCE) Model

2.1 Goddard Cumulus Ensemble (GCE) Model.

The GCE model, a CRM, has been developed and improved at NASA Goddard Space Flight Center over the past two and a half decades. The ability of the GCE model to simulate the impact of atmospheric aerosol concentrations on precipitation processes was recently enhanced (Tao *et al.* 2007) as were its abilities to account for the effects of land (Zeng *et al.* 2007) and ocean surface processes on convective systems in different geographic locations (Wang *et al.* 2003; Tao *et al.* 2004; Zeng *et al.* 2008). The GCE model's bulk microphysical scheme were recently modified to reduce the over-estimated and unrealistic amount of grauple

in the stratiform region (Tao *et al.* 2003; Lang *et al.* 2007), to better address saturation issues (Tao *et al.* 2003) and to obtain more realistic ice water contents for longer-term simulations (Zeng *et al.* 2008, 2009). Recently, the GCE model has been adapted to interface with a couple of other bulk microphysical schemes, namely the single and double moment versions of the Colorado State University (CSU) Regional Atmospheric Modeling System's (RAMS's) bulk microphysical scheme (Meyers *et al.* 1997; Saleeby and Cotton 2004), and a spectral bin microphysical scheme (Khain *et al.* 2004; Tao *et al.* 2007; Li *et al.* 2009a&b). The development and main features of the GCE model were published in Tao and Simpson (1993) and Tao *et al.* (2003). A review on the application of the GCE model to better understand precipitation processes can be found in Tao (2003). Table 2 shows the major characteristics of the GCE model.

2.2 *Goddard Unified Weather Research and Forecasting Model (WRF)*

The second component of the modeling system is WRF (Michalakes *et al.* 2004), a next-generation mesoscale forecast model and assimilation system developed at NCAR along with several NOAA and DOD partners. The model is designed to support research advancing the understanding and prediction of mesoscale precipitation systems. It incorporates advanced numerics and data assimilation techniques and has a multiple

Fig. 2 Schematic diagram showing planned components of the NASA unified WRF. The blue boxes represent physical processes (packages) developed by NASA scientists. The light green boxes represent the WRF dynamical core and others (*i.e.*, NCAR) developed outside of NASA. GOCART stands for Goddard Chemistry Aerosol Radiation and Transport model.

re-locatable nesting capability as well as improved physics. WRF will be used for a wide range of applications, from idealized research to operational forecasting, with an emphasis on horizontal grid sizes in the range of 1-10 km.

Various Goddard physical packages (*i.e.*, CRM-based microphysics, radiation and land-surface hydrology processes) as well as a real-time forecast system using Goddard Earth Observing System (GEOS) global analyses that have been developed at NASA have recently been implemented into WRF (Fig. 2). The CRM-based packages have improved forecasts (or simulations) of convective systems [*e.g.*, a linear convective system in Oklahoma (International H2O project, IHOP-2002), an Atlantic hurricane (Hurricane Katrina, 2005), high latitude snow events (Canadian CloudSat CALIPSO Validation Project, C3VP 2007), and a heavy orographic-related precipitation event in Taiwan (Summer 2007)]. In addition, two other GSFC modeling components have been coupled to the GSFC WRF representing the land surface (*i.e.*, the Land Information System or LIS) and aerosols [*i.e.*, the WRF Chemistry Model and Goddard Chemistry Aerosol Radiation and Transport Model (GOCART)].
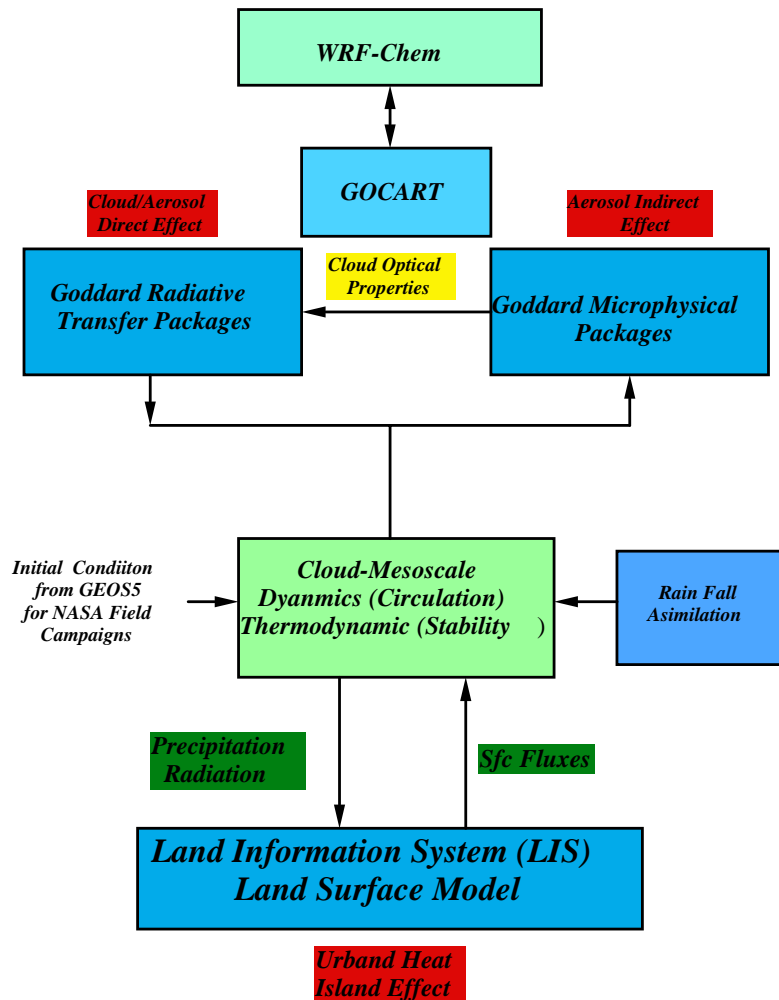
2.3 Goddard Multi-Scale Modeling Framework (MMF)

The third component of the modeling system couples the NASA Goddard finite volume GCM (fvGCM) with the GCE model (known as the Goddard MMF)[2]. The use of the fvGCM allows for global coverage and the use of the GCE for the explicit simulation of subgrid cloud processes and their interaction with radiation and surface processes. This modeling system has been applied to the study of climate scenarios such as the 1998 El Nino and 1999 La Nina. The new coupled modeling system results in the more realistic propagation and intensity of tropical rainfall systems and intra-seasonal oscillations and an improved diurnal variation of precipitation; all are difficult to capture using even state-of-the-art GCMs with subgrid convection schemes. The new Goddard MMF is the second MMF developed worldwide following the one at CSU. Despite differences in model dynamics and physics between the Goddard and CSU MMFs, both simulate stronger MJOs, better cloudiness (high and low), single ITCZs and more realistic diurnal rainfall patterns than traditional GCMs. Both MMFs also have similar biases, such as a summer precipitation bias (relative to observations and to their parent GCMs) in Asian monsoon regions. However, there are notable differences between the two MMFs. For example, the CSU MMF simulates less rainfall over land than its parent GCM, which is why it simulates less global rainfall than its parent GCM. The Goddard MMF simulates more global rainfall than its parent GCM because of a high contribution from its oceanic component. Please see Tao *et al.* (2009) for a detailed discussion.
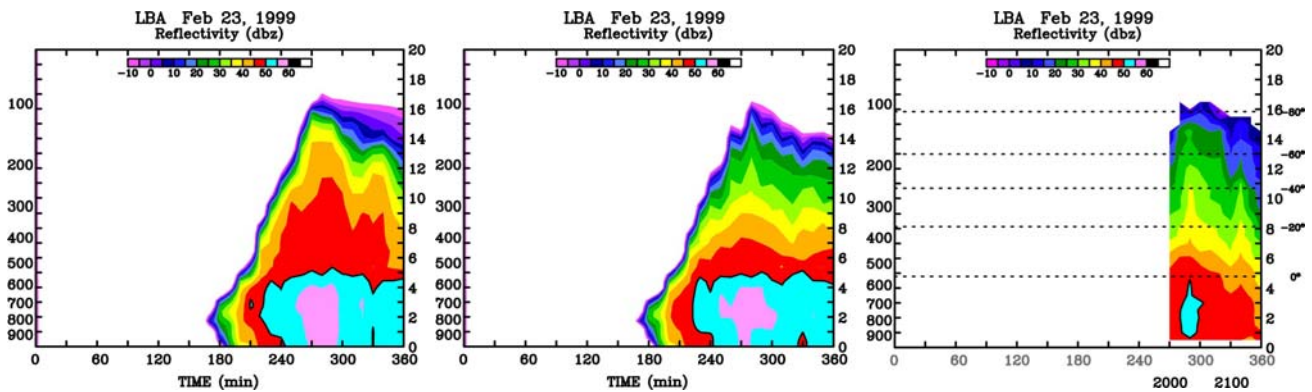

Fig. 3   Time-height cross sections of maximum radar reflectivity obtained from 3D simulations of the 23 February 1999 easterly regime event observed during TRMM LBA (Large Scale Biosphere-Atmosphere Experiment in Amazonia) using the original Rutledge and Hobbs (1984) based bulk microphysics formulation (left panel), an improved version (midde panel) and observed (right panel). Climatologically, 40-dBZ penetrations above 10 km are rare even over land (Zipser *et al.* 2006; Li *et al.* 2008). Ground-based radar data for this case indicated 40-dBZ echoes reached to approximately 8 km.

2.4 Goddard Satellite Data Simulation Unit (GSSU)

The Goddard SDSU is a multi-satellite simulator unit. It has six simulators at present: passive microwave, radar, visible-infrared spectrum, lidar, ISCCP type, and broadband (see Fig. 1). The SDSU can compute satellite-consistent radiances or backscattering signals from simulated atmospheric profiles and condensates consistent with the unified microphysics within the multi-scale modeling system (Fig. 1). These simulated radiances and backscattering signatures can be directly compared with satellite observations, establishing a satellite-based framework for evaluating the cloud parameterizations. This method is superior to the traditional method of validating models with satellite-based products, since models and satellite products often use different assumptions in their cloud microphysics (Matsui *et al.* 2009). Once the cloud

---

[2] The typical configuration for the Goddard MMF consists of the fvGCM run with 2.5° x 2° horizontal grid spacing with 32 layers from the surface to 0.4 hPa and the two-dimensional (2D) GCE using 64 horizontal grids (in the east-west orientation) and 32 levels with 4 km horizontal grid spacing and cyclic lateral boundaries. The time step for the 2D GCE is 10 seconds, and the fvGCM-GCE coupling interval is one hour, which is the fvGCM physical time step.

model reaches satisfactory agreement with the satellite observations, simulated clouds, precipitation, atmospheric states, and satellite-consistent radiances or backscattering will be provided to the science community as an *a priori* database for developing physically-based cloud and precipitation retrieval algorithms. Thus, the SDSU coupled with the multi-scale modeling system can lead to a better understanding of cloud processes in the Tropics as well as improved precipitation retrievals from current and future NASA satellite missions [*i.e.*, TRMM, the A-Train, GPM (Global Precipitation Measurement), and the ACE mission].

3. Results

3.1 The improvements of the microphysics scheme

There is a well-known bias common to many of the bulk microphysics schemes currently being used in cloud-resolving models. It involves the tendency for these schemes to produce excessively large

Fig. 4 Observed (left-top) and model simulated accumulated rainfall from August 6 0000UTC to August 9 0000UTC 2009. The original (right-top), improved (left-bottom) and warm rain only (right-bottom) are shown for comparison with observation.

reflectivity values (*e.g.*, 40 dBZ) in the middle and upper troposphere in simulated convective systems and is primarily due to excessive amounts and/or sizes of graupel (*e.g.*, Lang *et al.* 2007; Li *et al.* 2008). This bias is also related to a bias in excessive simulated ice scattering. The Rutledge and Hobbs (1983, 1984) based bulk microphysics scheme within the GCE model (Lang *et al.* 2011 and Fig. 3) and WRF (Tao *et al.* 2011 and Fig. 4) is modified to reduce this bias. Systematic evaluation of the scheme resulted in the following changes to individual processes: the efficiencies for snow and graupel riming and snow accreting cloud ice were lowered or made dependent on collector particle size, thresholds for converting rimed snow to graupel were tightened, snow and graupel were allowed to sublimate out of cloud, simple rime splintering, immersion freezing and contact nucleation parameterizations were added, the Fletcher (1962) curve for the number of activated ice nuclei was replaced with the Meyers *et al.* (1992) formulation throughout, the saturation adjustment scheme was relaxed to allow water saturation at colder temperatures and the presence of ice super saturation, ambient relative humidity and cloud ice size were accounted for in the "Bergeron" growth of cloud ice to snow, cloud ice fall speeds following Hong *et al.* (2004) were added and accounted for in the sweep volumes of processes accreting cloud ice, and the threshold for snow auto-conversion was changed to physical units. In addition, size-mapping schemes for snow and graupel were added whereby the characteristic size (*i.e.*, inverse of the slope parameter for the inverse exponential distributions) was specified based on temperature and mixing ratio, effectively lowering the size of particles at colder temperatures while still allowing particles to become larger near the melting level and at higher mixing ratios.

3.2 WRF simulated Typhoon Morakot case

In recent years, heavy rainfall associated with severe weather events (*e.g.*, typhoons, local heavy precipitation events) has caused significant damage to the economy and loss of human life throughout Taiwan. For example, Typhoon Morakot struck Taiwan on the night of Friday August 7th, 2009 as a Category 2 storm with sustained winds of 85 knots (92 mph). Although the center made landfall in Hualien county along the
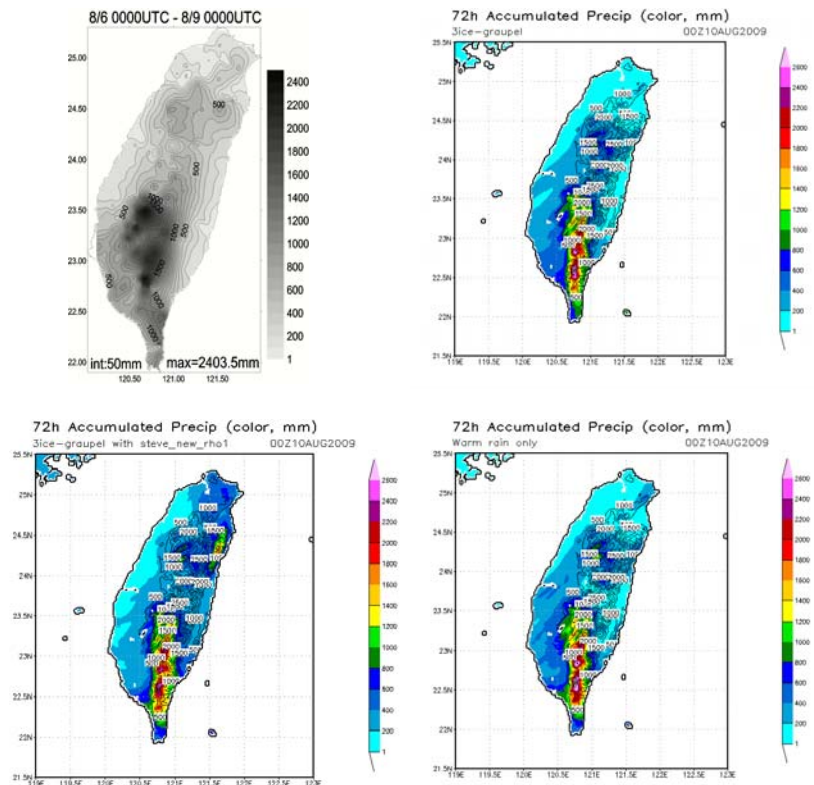
central east coast of Taiwan and passed over the central northern part of the island, it was southern Taiwan that received the worst effects of the storm where locally as much as 2400 mm of rain were reported, resulting in the worst flooding there in 50 years. The enormous amount of rain resulted in massive flooding and devastating mudslides. More than 600 people were confirmed dead (including hundreds of people in Shiao Lin Village, which was buried by a large mudslide).
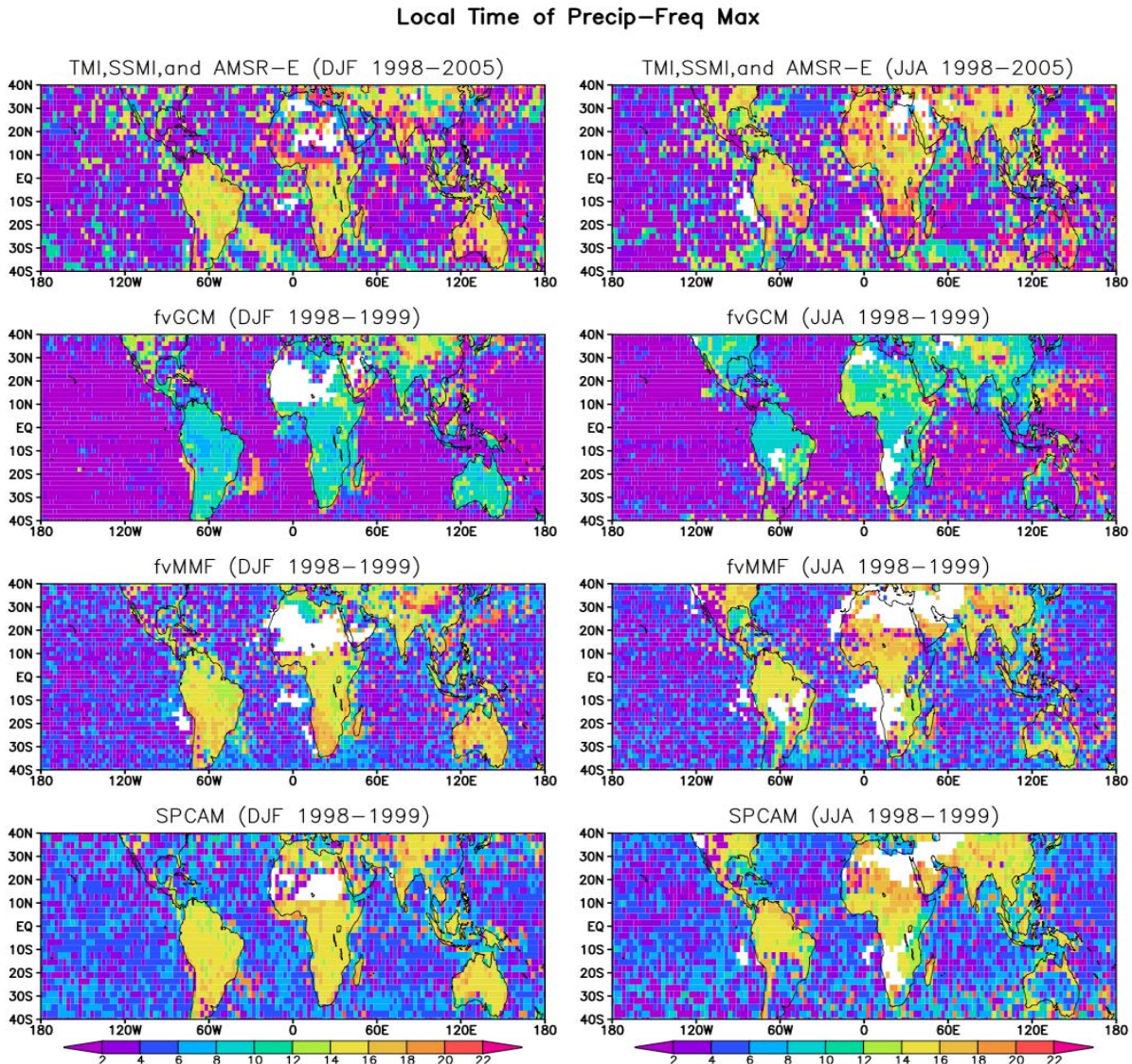

Fig. 5 Geographical distribution of the LST for the non-drizzle precipitation frequency maximum in winter (left panels) and summer (right panels) as observed by satellite from 1998-2005 (upper panels), simulated with the Goddard fvGCM (middle-upper panels) for two years (1998-1999), Goddard MMF (middle-lower panels) and CSU MMF (bottom panels). Blank regions indicate no precipitation. The MMF results are based on detailed 2D GCE model-simulated hourly rainfall output. Satellite retrieved rainfall is based on a 5-satellite constellation including the TRMM Microwave Imager (TMI), Special Sensor Microwave Imager (SSMI) from the Defense Meteorological Satellite Program (DMSP) F13, F14 and F15, and the Advanced Microwave Scanning Radiometer – Earth Observing System (AMSR-E) onboard the Aqua satellite.

Figure 4 shows the observed and WRF-simulated rainfall using three different options (improved and original 3ICE-graupel) and warm rain only in the Goddard microphysical scheme. Generally speaking, WRF produced the right distribution of precipitation for this typhoon case despite using different Goddard

microphysical options. For example, in all of the runs the main precipitation event is elongated in the southwest-northeast direction and concentrated in a heavy north-south line over southern Taiwan as observed. All options resulted in simulations wherein the main area of precipitation continued over southern Taiwan over the 72-h period. This feature also agrees with observations. The results (with high resolution visualization) show that a persistent (over 48 h) southwesterly flow associated with Morakot and its circulation was able to draw up copious amounts of moisture from the South China Sea into southern Taiwan where it was able to interact with the steep topography in all four microphysical options. These results suggest that the main rainfall distribution in the Morakot case is determined by the large-scale circulation pattern (*i.e.*, the typhoon-induced circulation). The interaction between the terrain and moisture flux was the dominant factor that led to the floods/landslides in this case. All of the options produced more than 2000 mm of accumulated rainfall over southern Taiwan. The improved 3ICE-graupel produced more rainfall over northeastern Taiwan, which may be in better agreement with observations than other schemes (see Fig. 4). In addition, the warm-rain-only produced almost similar results as other two cases in terms of rainfall pattern, maximum rainfall (> 2500 mm) and total amount rain over South Taiwan and whole Island (Fig. 4). These results suggested that the warm rain processes are dominant for precipitation processes.
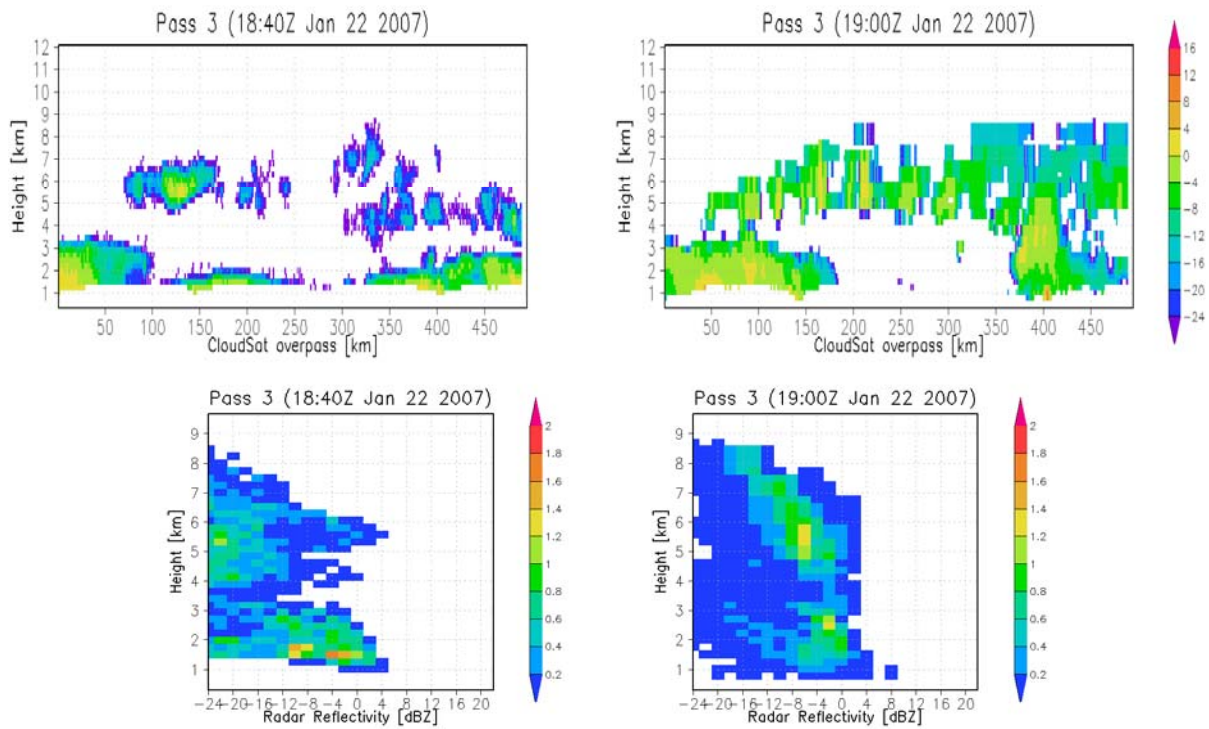

Fig. 6 Instantaneous cross-sectional snap shot (upper panels) and contoured frequency with altitude diagrams (CFADs) (lower panels) of CloudSAT-observed (left) and WRF-SDSU-simulated (right) Cloud Profiling Radar (CPR, 94 GHz) reflectivities.

3.3 MMF simulations of diurnal variation of precipitation systems

The diurnal cycle is a fundamental mode of atmospheric variability. Successful simulation of the diurnal variability of the hydrologic cycle and radiative energy budget provides a robust test of physical processes represented in atmospheric models (*e.g.*, Slingo 1987, Randall *et al.* 1991, Lin *et al.* 2000). Figure 5 shows the geographical distribution of the local solar time (LST) of the non-drizzle precipitation frequency maximum in winter and summer of 1998 as simulated by the fvGCM, fvMMF, and CSU MMF. Satellite microwave rainfall retrievals from a 5-satellite constellation are analyzed at 1-hour intervals from 1998 to 2005 for comparison. The non-drizzle precipitation is defined as precipitation that occurs such that the 1-hour averaged rain rate is larger than 1 mm/day (see Lin *et al.* 2007).

Satellite microwave rainfall retrievals in general show that precipitation occurs most frequently in the afternoon to early evening over the major continents such as South and North America, Australia, and west and central Europe, reflecting the dominant role played by direct solar heating of the land surface. Over open oceans, a predominant early morning maximum in rain frequency can be seen in satellite observations, consistent with earlier studies (see a review by Sui *et al.* 1997, 2008). The MMF is superior to the fvGCM in reproducing the correct timing of the late afternoon and early evening precipitation maximum over the land and the early morning precipitation maximum over the oceans. The fvGCM, in contrast, produces a dominant morning maximum rain frequency over major continents. Additional and more detailed comparisons between the observed and MMF-simulated diurnal variation of radiation fluxes, clouds and precipitation under different large-scale weather patterns and different climate regimes will be published elsewhere.

3.4 Evaluating model microphysics with the coupled satellite simulator

WRF, configured with the Goddard microphysics and radiation schemes, was used to simulate two snow events (January 20-22, 2007) over the C3VP site in Ontario, Canada (Shi *et al.* 2010). Figure 6 displays 94GHz radar reflectivities from CloudSAT observations and WRF-SDSU simulations. The cross-sectional comparison indicates that WRF successfully captured the spatial distribution of radar reflectivity, while the statistical comparison using contoured frequency with altitude diagrams (CFADs) shows that WRF overestimated radar reflectivity above 4 km. This result demonstrates that WRF was able to capture the cloud macro-structure reasonably well but not the cloud microphysics. An improved version of the microphysics is now being developed based largely on the comparison between model-simulated and satellite-observed cloud and precipitation properties (Matsui *et al.* 2009). Improved microphysics and hence model simulations are necessary to provide consistent 4D thermodynamic and dynamic cloud data sets for future GPM snow retrievals and to improve our understanding of precipitation processes over high-latitude regions.

4. Conclusions

Significant advances in the use of CRMs to simulate and improve our understanding of convective dynamics and its interaction with microphysics, precipitation, clouds, radiation, surface effects and boundary layers across multiple scales have been made over the past four decades. These model simulations are vital for comprehending the interaction between cloud systems and the large-scale circulation and also play a key role in the retrieval of precipitation and latent heating from satellite measurements (*i.e.*, Tao *et al.* 2006). The unified physics in the multi-scale modeling system is mainly based on those developed for the CRMs. However, the enormous dynamic range of modern CRMs presents new challenges for validation. This will involve integrated satellite simulators, satellite datasets, field-campaign analysis, CRMs, high-resolution NWP models (*i.e.*, WRF), and the MMF.

Global CRMs have already been run on an experimental basis, made possible by ever-improving computing power (Satoh *et al.* 2005). It is expected that by incorporating physical packages[3] originally developed for high-resolution process models such as CRMs into NWP models and GCMs along with the continuing development of global CRMs, the ability to simulate realistic weather and climate in the near future will be greatly enhanced (see Tao and Moncrieff 2009 for more discussion).

References

Fletcher, N. H., 1962: The Physics of Rain Clouds. Cambridge University Press, 386 pp.

---

[3] Note that the microphysics scheme and its interactions with radiation and surface processes are still the major uncertainty and need to be developed, improved and validated.

GEWEX Cloud System Study (GCSS), 1993: *Bull. Amer. Meteor. Soc.,* **74**, 387-400.

Hong, S.-Y., J. Dudhia, and S.-H. Chen, 2004: A revised approach to ice microphysical processes for the bulk parameterization of clouds and precipitation. *Mon. Wea. Rev.,* **132**, 103-120.

Khain, A., A. Pokrovsky, M. Pinsky, A. Seigert, and V. Phillips, 2004: Simulation of effects of atmospheric aerosols on deep turbulent convective clouds using a spectral microphysics mixed-phase cumulus cloud model. Part I: Model description and possible applications. *J. Atmos. Sci.,* **61**, 2983-3001.

Lang, S., W.-K. Tao, R. Cifelli, W. Olson, J. Halverson, S. Rutledge, and J. Simpson, 2007: Improving simulations of convective system from TRMM LBA: Easterly and Westerly regimes. *J. Atmos. Sci.,* **64**, 1141-1164.

Lang, S., W.-K. Tao, X. Zeng, and Y. Li, 2011: Reducing the biases in simulated radar reflectivities from a bulk microphysics scheme: Tropical convective systems, *J. Atmos. Sci.*, (submitted).

Li, X, W.-K. Tao, A. Khain, J. Simpson, and D. E. Johnson, 2009a: Sensitivity of a cloud-resolving model to bulk and explicit bin microphysical schemes. Part I: Comparisons. *J. Atmos. Sci.*, **66**, 3-21.

Li, X., W.-K. Tao, A. P. Khain, J. Simpson, and D. E. Johnson, 2009b: Sensitivity of a cloud-resolvong model to the bulk and explicit bin microphysical schemes. Part II: Cloud microphysics and storm dynamics interactions. *J. Atmos. Sci.*, **66**, 22-40.

Li, Y., E. J. Zipser, S. K. Krueger, and M. A. Zulauf, 2008: Cloud-resolving modeling of deep convection during KWAJEX. Part I: Comparison to TRMM satellite and ground-based radar observations. *Mon. Wea. Rev.*, **136**, 2699-2712.

Lin, X., D. A. Randall, and L. D. Fowler, 2000: Diurnal variability of the hydrological cycle and radiative fluxes: Comparisons between observations and a GCM. *J. Climate*, **13**, 4159-4179.

Lin, X., S. Q. Zhang, and A. Y. Hou, 2007: Variational assimilation of global microwave rainfall retrievals: Physical and dynamical impact on GEOS analyses. *Mon. Wea. Rev.*, **135**, 2931-2957.

Matsui, T., X. Zeng, W.-K. Tao, H. Masunaga, W. S. Olson, and S. Lang, 2009: Evaluation of long-term cloud-resolving model simulations using satellite radiance observations and multi-frequency satellite simulators. *J. Atmos. Oce. Tech.* **26**, 1261-1274.

Meyers, M. P., P. J. DeMott, and W. R. Cotton, 1992: New primary ice-nucleation parameterizations in an explicit cloud model. *J. Appl. Meteor.*, **31,**708–721.

Meyers M. P., R. L. Walko, J. Y. Harrington, and W. R. Cotton, 1997: New RAMS cloud microphysics. Part II: The two-moment scheme. *Atmos. Res.*, **45**, 3–39.

Michalakes, J., J. Dudhia, D. Gill, T. Henderson, J. Klemp, W. Skamarock, and W. Wang, 2004: The Weather Research and Forecast Model: Software architecture and performance. The 11th ECMWF Workshop on the Use of High Performance Computing in Meteorology. 25–29 October 2004, Reading, U.K., Ed. George Mozdzynski.

Nasuno, T., H. Tomita, S. Iga, H. Miura, and M. Satoh (2008), Multi-scale organization of convection simulated with explicit cloud processes on an aquaplanet. *J. Atmos. Sci.*, **65**, 1246-1265.

Randall, D., A. Harshvardhan, and D. A. Dazlich, 1991: Diurnal variability of the hydrologic cycle in a general circulation model. *J. Atmos. Sci.*, **48**, 40-62.

Rutledge, S. A., and P. V. Hobbs, 1983: The mesoscale and microscale structure of organization of clouds and precipitation in midlatitude cyclones. VIII: A model for the "seeder-feeder" process in warm-frontal rainbands. *J. Atmos. Sci.*, **40**, 1185–1206.

Rutledge, S. A., and P. V. Hobbs, 1984: The mesoscale and microscale structure and organization of clouds and precipitation in midlatitude cyclones. Part XII: A diagnostic modeling study of precipitation development in narrow cold-frontal rainbands. *J. Atmos. Sci.,* **41**, 2949-2972.

Saleeby S. M., and W. R. Cotton, 2004: A large droplet mode and prognostic number concentration of cloud droplets in the Colorado State University Regional Atmospheric Modeling System (RAMS). Part I: Module descriptions and supercell test simulations. *J. Appl. Meteor.*, **43**, 182–195.

Satoh, M., H. Tomita, H. Miura, S. Iga1 and T. Nasuno, 2005: Development of a global cloud resolving model – a multi-scale structure of tropical convections – *J. of the Earth Simulator*, **Volume 3**, 1-9.

Shi, J. J., W.-K. Tao, T. Matsui, A. Hou, S. Lang, C. Peters-Lidard, G. Jackson, R. Cifelli, S. Rutledge, and W. Petersen, 2010: Microphysical Properties of the January 20-22 2007 Snow Events over Canada: Comparison with in-situ and Satellite Observations. *J. Applied Meteor., Climatol.*, **49**, 2246-2266.

Slingo, A., R. C. Wilderspin, and S. J. Brentnall, 1987: Simulation of the diurnal cycle of outgoing longwave radiation with an atmospheric GCM. *Mon. Wea. Rev.,* **115,** 1451–1457.

Sui, C.-H., K.-M. Lau, Y. Takayabu, and D. Short, 1997: Diurnal variations in tropical oceanic cumulus convection during TOGA COARE. *J. Atmos. Sci.*, **54**, 637-655.

Sui, C.-H., X. Li, K.-M. Lau, W.-K. Tao, M.-D. Chou, and M.-J. Yang, 2008: Convective-radiative-mixing processes in the Tropical Ocean-Atmosphere. *Recent Progress in Atmospheric Sciences with Applications to the Asia-Pacific Region*, K.-N. Liou and M.-D. Chou (eds), World Scientific, 66-88.

Tao, W.-K., and J. Simpson, 1993: The Goddard Cumulus Ensemble Model. Part I: Model description. *Terrestrial, Atmospheric and Oceanic Sciences*, **4**, 19-54.

Tao, W.-K, 2003: Goddard Cumulus Ensemble (GCE) model: Application for understanding precipitation processes. *Cloud Systems, Hurricanes, and the Tropical Rainfall Measuring Mission (TRMM): A Tribute to Dr. Joanne Simpson*, *Meteor. Monogr.,* **51**, *Amer. Meteor. Soc*, 107-138.

Tao, W.-K., J. Simpson, D. Baker, S. Braun, M.-D. Chou, B. Ferrier, D. Johnson, A. Khain, S. Lang, B. Lynn, C.-L. Shie, D. Starr, C.-H. Sui, Y. Wang, and P. Wetzel (2003), Microphysics, radiation and surface processes in the Goddard Cumulus Ensemble (GCE) model. *Meteorol. Atmos. Phys., 82,* 97-137.

Tao, W.-K., D. Johnson, C.-L. Shie, and J. Simpson. 2004: Atmospheric energy budget and large-scale precipitation efficiency of convective systems during TOGA COARE, GATE, SCSMEX and ARM: Cloud-resolving model simulations, *J. Atmos. Sci.*, **61**, 2405-2423.

Tao, W.-K., E. Smith, R. Adler, Z. Haddad, A. Hou, T. Iguchi, R. Kakar, T.N. Krishnamurti, C. Kummerow, S. Lang, R. Meneghini, N. Nakamura, T. Nakazawa, K. Okamoto, W. Olson, S. Satoh, S. Shige, J. Simpson, Y. Takayabu, G. Tripoli, and S. Yang, 2006: Retrieval of latent heating from TRMM measurements, *Bull. Amer. Meteor. Soc.,* **87,** 1555-1572.

Tao, W.-K., 2007: Cloud Resolving Modeling. *J. Meteor. Soc. Japan*, Special Issue of 125th Anniversary of Japan Meteorology Society**, 85**, 305-330.

Tao, W.-K., X. X. Li, A. Khain, T. Matsui, S. Lang, and J. Simpson, 2007: The role of atmospheric aerosol concentration on deep convective precipitation: Cloud-resolving model simulations*. J. Geophy. Res.,* **112**, D24S18, doi:10.1029/2007JD008728.

Tao, W.-K., J. Chern, R. Atlas, D. Randall, X. Lin, M. Khairoutdinov, J._L. Li, D. E. Waliser, A. Hou, C. Peters-Lidard, W. Lau, and J. Simpson, 2009: Multi-scale modeling system: Development, applications and critical issues, *Bull. Amer. Meteor. Soc., **90**,* 515-534. Available at http://ams.allenpress.com/perlserv/?request=get-toc-aop&issn=1520-0477

Tao, W.-K., and M. Moncrieff, 2003: Cloud Modeling, *Encyclopedia of Atmospheric Sciences*, Edited by J. Holton, J. Curry and J. Pyle, 539-548.

Tao, W.-K., and M. Moncrieff, 2009: Multi-scale cloud-system modeling. *Reviews of Geophysics*. **47**, RG4002, doi:10.1029/2008RG000276.

Wang, Y., W.-K. Tao, J. Simpson, and S. Lang, 2003: The sensitivity of tropical squall lines (GATE and TOGA COARE) to surface fluxes: 3-D Cloud resolving model simulations, *Q. J. R. Met. Soc.,* **129**, 987-1007.

Zeng, X., W.-K. Tao, M. Zhang, S. Lang, C. Peters-Lidard, J. Simpson, S. Xie, S. Kumar, J. V. Geiger, C.-L. Shie, and J. L.. Eastman, 2007: Evaluation of long-term cloud-resolving modeling with observational cloud data. *J. Atmos. Sci.,* **64**, 4153–4177.

Zeng, X., W.-K. Tao, S. Lang, A. Hou, M. Zhang, and J. Simpson, 2008: On the sensitivity of Atmospheric ensemble to cloud microphysics in long-term cloud-resolving model simulations. *J. Meteor. Soc. Japan*, *Special Issue on high-resolution cloud models*, *J. Meteor. Soc. Japan*, **86A**, 45-65.

Zeng, X., W.-K. Tao, M. Zhang, A. Y. Hou, S. Xie, S. Lang, X. Li, D. Starr, X. Li, and J. Simpson, 2009: The indirect effect of ice nuclei on atmospheric radiation. *J. Atmos. Sci.,* **66**, 41-61.

Zipser, E. J., D. J. Cecil, C. Liu, S. W. Nesbitt, and D. P. Yorty, 2006: Where are the most intense thunderstorms on Earth? *Bull. Amer. Meteor. Soc.*, **87**, 1057-1071.